

Unmanned Aircraft Flight Control Aided by Phased-Array Radio Navigation

Kristoffer Gryte Torleiv H. Bryne Tor Arne Johansen

Department of Engineering Cybernetics
Centre for Autonomous Marine Operations and Systems
Norwegian University of Science and Technology, NTNU
Trondheim, Norway
gryte@ieee.org

Abstract

Navigation systems of safety-critical unmanned aircraft need an alternative position aiding source to global navigation satellite system. One promising alternative, is position measurements from phased-array radio systems. The presented navigation system consist of a multiplicative extended Kalman filter that utilize these measurements, along with an exogenous altitude measurement, to aid an inertial navigation system. The reliability and accuracy of the navigation system is demonstrated through beyond-visual-line-of-sight flights with a fixed-wing UAV, without the use of global navigation satellite systems. This uses a conventional guidance controller module, which also monitor the navigation quality.

1 Introduction

The discontinuation of the selective availability pseudorandom errors in global position system (GPS) in year 2000 laid the foundation for a boost in the use of global navigation satellite systems (GNSS) for many applications, such as navigation of manned and unmanned vehicles. Through the standard positioning services and differential correction services, GNSS has the advantage of providing high-accuracy positioning, navigation and timing (PNT) signals, with global coverage, through lightweight receivers at a low cost to the user. GNSS has proved particularly useful when integrated with an inertial measurement unit (IMU) with its complementary features such as high precision, albeit with a bias, and high sampling frequency, making it possible to obtain high accuracy, high precision position estimates at a high rate. However, when designing safety-critical systems, it is important to keep in mind the weaknesses of GNSS. The low signal power makes GNSS highly susceptible to radio frequency interface (RFI), both natural RFI, such as ionospheric scintillations (Yeh and Liu, 1982) and multipath, and intentional RFI, such as jamming (Pinker and Smith, 1999) and spoofing (Kerns et al., 2014; Schmidt et al., 2016). The worst-case scenario of RFI is exemplified by the 2011 spoofing incident where Iranian forces successfully captured a U.S. RQ-170 UAV (Jaffe and Erdbrink, 2011). Another aspect is the fact that the complex GNSS satellite systems are controlled by international bodies, and is believed to be one of the first systems to become unavailable in the event of a large international conflict. The complexity of these systems was showcased in July 2019, when it took the European Global Navigation Satellite System Agency (GSA) a week to fix and restore the Galileo satellite system PNT service (Karasz, 2019). With this in mind, it is clear that GNSS should be considered as a nice-to-have feature, and that it, in itself, cannot be relied upon for navigation of safety critical systems.

The need for a reliable alternative for safety critical applications motivates research into alternative, GNSS-free navigation solutions, of which there are many. As GNSS rely on multilateration of pseudorange mea-

measurements, the instinctive solution to GNSS-free navigation is to rely on range measurements from other sources (Djugash et al., 2009), such as radio navigation (Gezici et al., 2005; Mahfouz et al., 2008). The main drawback is the need for local infrastructure, as three or more ground fixed antennas will be needed. Another option that requires local infrastructure is ground based radar positioning. This will also require a radio link to send the tracking data to the UAV. Visual odometry (Forster et al., 2014; Mourikis and Roumeliotis, 2007), visual SLAM (Engel et al., 2014; Mur-Artal et al., 2015) and terrain/map matching (Gustafsson, 2010) all rely on tracking of multiple features, are self-contained solutions that do not need any infrastructure, but are either limited to local navigation or require a global map.

Another alternative is position measurements from a phased-array radio system (PARS). PARS is primarily designed as a high-bandwidth radio communication link, providing the user with e.g. telemetry data from a UAV, including a live video streams (Hovstein et al., 2014), as well as relaying information through a UAV to units that themselves are beyond-radio-line-of-sight from the base antenna. As opposed to omnidirectional alternatives, PARS transmits a directed, narrow beam that allows for high transmission power and long range. Information from this directed beam can be used to deduce the position of the radio, relative to the ground station (Albrektsen et al., 2018a), similar to standard radar tracking calculations (Bar-Shalom et al., 2011), but with a trivial data association step. While PARS does depend on local infrastructure, only a single ground antenna is needed to provide a full 3D position measurement.

Previous work with PARS initially focused on data collection, using fixed-wing UAVs, and assessment of the data (Albrektsen et al., 2018a; Albrektsen et al., 2018b; Albrektsen et al., 2017). The first navigation results were obtained using a nonlinear observer, relying on measurements from the PARS, exogenous altitude and a magnetometer. Later (Gryte et al., 2019; Gryte, 2020), the nonlinear observer was replaced with an indirect multiplicative extended Kalman filter (MEKF), which improved the position accuracy. The covariance estimates in the Kalman filter also laid the foundation for outlier rejection of the PARS measurements, and enabled heading estimation without the need for a magnetometer, through the coupling of the angular and translational error dynamics and sufficient excitation. In (Gryte et al., 2019), the MEKF was implemented on a real-time system onboard a multicopter UAV, to provide position estimates online for demonstration purposes.

This research seeks to prove our hypothesis that the estimates provided by the PARS-aided inertial navigation system (INS) developed in (Gryte, 2020; Gryte et al., 2019) have the high precision and low latency required for closed-loop feedback on a fixed-wing UAV flying beyond-visual-line-of-sight (BVLOS) over open waters. This is achieved through design and implementation of a guidance, navigation and control (GNC) system, based on the PARS navigation system, used to control the UAV. This system also contributes to the airworthiness of the platform by providing safety mechanisms to monitor its state, and builds on existing, well-tested solutions, in a non-intrusive manner. The presented solution can be seen as a GNSS-free GNC system opposite to that used for indoor and underground applications, e.g. (Khattak et al., 2019; Mohta et al., 2017): Such environments are usually cluttered and hence provides many features for the visual sensors, albeit putting high demands on control and collision avoidance. The scenario presented here is less challenging in terms of control, but the sea surface makes feature detection difficult using visual systems to aid the navigation system. To the best of our knowledge, this system is the first successful civilian GNSS-free UAV GNC system deployed in BVLOS flight in controlled airspace.

After presenting the notation and some mathematical preliminaries in Section 2, the article starts by presenting the principles behind PARS in Section 3, and how it can be used to provide position measurements. The navigation system is presented in Section 4 in brevity, before Section 5 explains how it is integrated with the safety mechanisms, and with the guidance controllers to allow safe testing. Section 6 presents the results from three different experiments, where the PARS-based navigation system is deployed on a fixed-wing UAV. The first experiment demonstrates the robustness of the navigation system to loss of PARS measurements by showing how the INS estimates evolve after the disconnection of the PARS measurement, and how the estimates recover once the PARS-positioning solution is recovered. The second experiment investigates how the guidance controllers perform when switching navigation source. The third experiment include the results from a BVLOS flight of about 20 km in lawnmower pattern, over open water, with a maximum distance of

5 km from the ground radio station.

2 Preliminaries

2.1 Notation

The Euclidean vector norm is denoted $\|\bullet\|_2$, where \bullet is the variable placeholder. The $n \times n$ identity matrix is denoted \mathbf{I}_n . The transpose of a vector or a matrix is denoted $(\bullet)^\top$, while $(\bullet)^H$ denotes the conjugate transpose. Coordinate frames are denoted with $\{\cdot\}$. $\mathbf{S}(\bullet) \in SS(3)$ represents the skew symmetric matrix such that $\mathbf{S}(\mathbf{z}_1)\mathbf{z}_2 = \mathbf{z}_1 \times \mathbf{z}_2$ for two vectors $\mathbf{z}_1, \mathbf{z}_2 \in \mathbb{R}^3$. $\mathbf{z} = (\mathbf{z}_1; \mathbf{z}_2; \dots; \mathbf{z}_n)$ denotes a vector of stacked column vectors $\mathbf{z}_1, \mathbf{z}_2, \dots, \mathbf{z}_n$. Furthermore, error variables are represented with $\delta\bullet$. In addition, $\mathbf{z}_{\gamma\beta}^\zeta \in \mathbb{R}^3$ denotes a vector \mathbf{z} , to frame $\{\beta\}$, relative $\{\gamma\}$, decomposed in $\{\zeta\}$. The $\text{diag}(\bullet, \dots, \bullet)$ function places the n arguments on the diagonal of a square matrix with n rows and n columns. Moreover, $\varepsilon_\bullet \sim \mathcal{N}(0, \sigma_\bullet^2)$ denotes Gaussian white noise with standard deviation σ_\bullet and $\mathbb{E}[\bullet]$ denotes the expected value. Furthermore, T_s represent the sampling time or step length in numerical integration methods. The imaginary unit is denoted j .

2.2 Coordinate Frames

This paper considers three coordinate frames. The first two are the Earth-fixed, non-rotating North East Down (NED) frame and the BODY reference frame, denoted $\{n\}$ and $\{b\}$, respectively. The NED directions are denoted N, E, D. The third coordinate system is the PARS ground radio antenna coordinate system, denoted $\{r\}$. This coordinate system is another NED frame.

2.3 Attitude representations and relationships

The primary attitude representation in this article is the unit quaternion, using the Hamiltonian representation, given as

$$\mathbf{q}_\beta^\gamma = \begin{pmatrix} q_s \\ \mathbf{q}_v \end{pmatrix} = \begin{pmatrix} q_s \\ q_x \\ q_y \\ q_z \end{pmatrix} \in \mathcal{Q} \quad (1)$$

where the set \mathcal{Q} is defined according to (Fossen, 2011) as

$$\mathcal{Q} := \{\mathbf{q}_\beta^\gamma \mid (\mathbf{q}_\beta^\gamma)^\top \mathbf{q}_\beta^\gamma = 1, \mathbf{q}_\beta^\gamma = (q_s; \mathbf{q}_v), q_s \in \mathbb{R}^1, \mathbf{q}_v \in \mathbb{R}^3\} \quad (2)$$

Conforming to Gade's notation (Gade, 2018), the quaternion can be used to calculate the rotation matrix, $\mathbf{R}_{\gamma\beta} \in SO(3)$,

$$\mathbf{R}_{\gamma\beta}(\mathbf{q}_\beta^\gamma) = (q_s - \mathbf{q}_v^\top \mathbf{q}_v) \mathbf{I}_3 + 2q_s \mathbf{S}(\mathbf{q}_v) + 2\mathbf{q}_v \mathbf{q}_v^\top, \quad (3)$$

as in e.g. (Markley, 2003, Eq. (4)) and (Farrell, 2008, App. D.2).

The Hamiltonian quaternion product, denoted \otimes , is given such that (Sola, 2015, Sec. 1.2.2)

$$\mathbf{q}_3 = \mathbf{q}_1 \otimes \mathbf{q}_2 = \begin{pmatrix} q_{1s}q_{2s} - \mathbf{q}_{1v}^\top \mathbf{q}_{2v} \\ q_{1s}\mathbf{q}_{2v} + q_{2s}\mathbf{q}_{1v} + \mathbf{S}(\mathbf{q}_{1v})\mathbf{q}_{2v} \end{pmatrix}. \quad (4)$$

The Euler angles (roll, pitch and yaw) are denoted

$$\Theta = (\phi, \theta, \psi)^\top. \quad (5)$$

2.4 Kinematics – Strapdown equations

The position and linear velocity of the BODY frame relative the NED frame is represented as $\mathbf{p}_{nb}^n \in \mathbb{R}^3$, $\mathbf{v}_{nb}^n \in \mathbb{R}^3$. The rotation of the body about the NED frame is parameterized with the unit quaternion \mathbf{q}_b^n . The angular velocity of BODY w.r.t. to NED is given as $\boldsymbol{\omega}_{nb}^b \in \mathbb{R}^3$, while the gravity vector is given as \mathbf{g}_b^n . With this stated, the resulting strapdown equations follows

$$\begin{aligned}\dot{\mathbf{p}}_{nb}^n &= \mathbf{v}_{nb}^n \\ \dot{\mathbf{v}}_{nb}^n &= \mathbf{R}_{nb}(\mathbf{q}_b^n) \mathbf{f}_{nb}^b + \mathbf{g}_b^n \\ \dot{\mathbf{q}}_b^n &= \frac{1}{2} \boldsymbol{\Omega}(\boldsymbol{\omega}_{nb}^b) \mathbf{q}_b^n\end{aligned}\quad (6)$$

based on the underlying assumption above that this NED frame is assumed to be inertial, where,

$$\mathbf{f}_{nb}^b = \mathbf{R}_{nb}^T(\mathbf{q}_b^n) (\dot{\mathbf{v}}_{nb}^n - \mathbf{g}_b^n). \quad (7)$$

represent the specific force.

3 Phased-array radio systems

PARS is primarily designed for communication, where the narrow beam shape allows for high power transmission. In its simplest form, a uniform linear array of D antennas, separated by a distance d_{tx} , the transmission direction Ψ_{tx} can be controlled by adjusting the phase shift for each antenna (Maruyama et al., 2016). The transmitted signal is delayed by an additional δ_t for each antenna, such that the phase shift from one antenna to the next is the same for all the antennas. From Figure 1a it is clear that

$$\sin \Psi_{tx} = \frac{\delta_t c}{d_{tx}}, \quad (8)$$

where $c = f\lambda$ is the signal speed, expressed in terms of frequency f and wavelength λ . Rearranging, and realizing that phase can be expressed in terms of time delay through $\phi = 2\pi f\delta_t$, results in

$$\Psi_{tx} = \arcsin\left(\frac{\phi\lambda}{2\pi d_{tx}}\right). \quad (9)$$

The inverse problem, estimating the direction Ψ_{rx} of a received signal based on its phase shift at the different antennas in the array, see Figure 1a, is known as the direction-of-arrival (DoA) problem (Chung et al., 2014; Haardt et al., 2014), which is based on the measurement model

$$\begin{aligned}\mathbf{X} &= \mathbf{C}\mathbf{F} + \mathbf{W} \\ \begin{bmatrix} X_1 \\ \vdots \\ X_M \end{bmatrix} &= \begin{bmatrix} a(\boldsymbol{\theta}_1) & \cdots & a(\boldsymbol{\theta}_D) \end{bmatrix} \begin{bmatrix} F_1 \\ \vdots \\ F_D \end{bmatrix} + \begin{bmatrix} W_1 \\ \vdots \\ W_M \end{bmatrix},\end{aligned}\quad (10)$$

which assumes far-field signal sources. The vector of measurements, \mathbf{X} , contains the signals measured at all the M antennas. They measure how the D signals in \mathbf{F} are affected by the accompanying steering vector $a(\boldsymbol{\theta}_i)$ and the additive noise \mathbf{W} . Here, i is the index representing one of the D transmitting antenna arrays. The steering vector is a known function of the variable vector $\boldsymbol{\theta}_i$, to be identified. For the simplest case of a linear, equidistant array, the steering vector is only dependent on $\boldsymbol{\theta}_i = [\Psi_{rx,i}]$, and can be expressed as

$$a(\boldsymbol{\theta}_i) = \left[1, e^{-j2\pi f_c \frac{d_{rx} \cos(\Psi_{rx,i})}{c}}, e^{-j2\pi f_c \frac{2d_{rx} \cos(\Psi_{rx,i})}{c}}, \dots, e^{-j2\pi f_c \frac{(M-1)d_{rx} \cos(\Psi_{rx,i})}{c}} \right]. \quad (11)$$

The DoA problem for estimating Ψ_{rx} (Krim and Viberg, 1996) can be solved by e.g. MUSIC (Schmidt, 1986), ESPRIT (Roy and Kailath, 1989) and SAMV (Abeida et al., 2013).

3.1 PARS for UAV navigation

As $\boldsymbol{\theta}_{\text{sph}} = [\Psi_{\text{rx}}, \alpha_{\text{rx}}, \rho]$, i.e. the azimuth angle, elevation angle and geometric range, whose computation is inherent to the PARS communication solution, represent a full 3D position of the transmitting antenna in the frame of the receiving antenna, it can also be used as a position measurement for a UAV. However, (Albrektsen et al., 2018a) showed that during flights over water, the PARS measurements are susceptible to multipath reflections from the sea surface. As the PARS system used was optimized for communication, this caused the tracked signal to jump from one cluster of measurements to another, when the signal strength of a reflected signal became stronger than the original signal. The phenomenon is particularly visible in the elevation measurements, that from time to time would alternate between the correct elevation angle and a non-physical downward-directed angle. To mitigate this, (Albrektsen et al., 2018a) suggest to instead use the PARS measurements in combination with an exogenous altitude measurement, e.g. from a barometer, instead of the error prone elevation angle measurement, resulting in cylindrical-coordinates-based PARS positioning. The geometric range and the azimuth angle are in the following assumed to originate from any DoA algorithm on the basis of (10), and are, along with the exogenous altitude measurement, assumed to be affected by additive noise, according to

$$y_\rho = \rho_u + \varepsilon_\rho, \quad (12)$$

$$y_\Psi = \Psi_u + \varepsilon_\Psi, \quad (13)$$

$$y_{\text{alt}} = -p_{nb,z,\text{exo}}^n + \varepsilon_{\text{alt}}, \quad (14)$$

with $\varepsilon_\bullet \sim \mathcal{N}(0, \sigma_\bullet^2)$. Here the subscript u symbolizes the UAV, while Ψ_u is shorthand notation for $\Psi_{\text{rx},1}$, assuming that a single UAV is the only transmitting source. The exogenous height measurement is denoted $-p_{nb,z,\text{exo}}^n$. Furthermore

$$\begin{aligned} \rho_u &= \|\mathbf{p}_{\text{PARS}}^r\|_2, \\ &= \sqrt{(p_{rb,x}^r)^2 + (p_{rb,y}^r)^2 + (p_{rb,z}^r)^2}, \end{aligned} \quad (15)$$

$$\Psi_u = \text{atan2}(p_{rb,y}^r, p_{rb,x}^r), \quad (16)$$

$$(17)$$

where $\mathbf{p}_{\text{PARS}}^r = (p_{rb,x}^r \ p_{rb,y}^r \ p_{rb,z}^r)$ is the true position of the UAV in the $\{r\}$ -frame, see Figure 1. As the elevation angle is discarded, the geometric range measurement must be projected into the horizontal plane for the triplet range, azimuth angle and altitude to constitute a valid 3D position. The horizontal range \bar{y}_ρ is a measurement of

$$\bar{\rho}_u = \sqrt{(p_{rb,x}^r)^2 + (p_{rb,y}^r)^2}, \quad (18)$$

derived as

$$\bar{y}_\rho = \sqrt{y_\rho^2 - y_{\text{alt}}^2} \quad (19)$$

An illustration of the geometric range ρ_u , horizontal range $\bar{\rho}_u$, elevation angle α_u and azimuth angle Ψ_u , relative to the $\{r\}$ -frame, can be seen in Figure 1b.

As shown in (Gryte, 2020), the cylindrical-coordinates-based PARS position measurement can be transformed to Cartesian coordinates, in the ground radio antenna frame, using

$$\bar{\mathbf{p}}_{\text{PARS}}^r = \begin{pmatrix} b_{\rho/\text{alt}}^{-1} b_\Psi^{-1} \bar{y}_\rho \cos(y_\Psi) \\ b_{\rho/\text{alt}}^{-1} b_\Psi^{-1} \bar{y}_\rho \sin(y_\Psi) \\ y_{\text{alt}} \end{pmatrix}, \quad (20)$$

where the measurements have been debiased according to (Bar-Shalom et al., 2011, Section 1.7.4), with biases $b_{\rho/\text{alt}} \approx 1$, following from the Monte-Carlo simulation in (Gryte, 2020, App. B), and $b_\Psi = \mathbb{E}[\cos(\varepsilon_\Psi)] = e^{-\sigma_\Psi^2/2}$, to account for the nonlinear mapping from cylindrical to Cartesian coordinates. In addition to

improving the accuracy, the debiasing makes the measurement noise less colored and thus more appropriate for Kalman filtering. The debiased PARS position measurement can then be transformed into the $\{n\}$ frame using

$$\mathbf{y}_{\text{PARS}}^n = \mathbf{R}_{nr}(\Theta_{\text{PARS}})\bar{\mathbf{p}}_{\text{PARS}}^T, \quad (21)$$

where Θ_{PARS} represents rotation angles of $\{r\}$ about $\{n\}$. Θ_{PARS} is obtained from pose calibration of the PARS ground antenna (Albrektsen et al., 2017).

In addition to the position measurement itself, the Kalman filter relies on knowledge of the covariance of the position measurement to estimate the position. The additive noise in (12) to (14), $\boldsymbol{\varepsilon} = (\varepsilon_\rho; \varepsilon_\Psi; \varepsilon_{\text{alt}})$, originates from the cylindrical position measurements, and must thus be mapped into the Cartesian $\{n\}$ frame through the similarity transform

$$\mathcal{R}_{\text{pars}}[k] = \mathbf{R}_{nr}(\Theta_{\text{PARS}})\mathbf{M}[k]\mathcal{R}_c[k]\mathbf{M}^\top[k]\mathbf{R}_{nr}^\top(\Theta_{\text{PARS}}), \quad (22)$$

to obtain the linearized measurement covariance matrix $\mathcal{R}_{\text{pars}}$, in the $\{n\}$ frame, where

$$\mathcal{R}_c[k] = \text{diag}(\mathbb{E}[\varepsilon_\rho^2[k]], \mathbb{E}[\varepsilon_\Psi^2[k]], \mathbb{E}[\varepsilon_{\text{alt}}^2[k]]) \quad (23)$$

is the covariance matrix in cylindrical coordinates, and

$$\mathbf{M} = \frac{\partial \bar{\mathbf{p}}_{\text{PARS}}^T}{\partial \boldsymbol{\varepsilon}} = \begin{pmatrix} m_{11} & m_{12} & m_{13} \\ m_{21} & m_{22} & m_{23} \\ 0 & 0 & 1 \end{pmatrix} \quad (24)$$

with

$$\begin{aligned} m_{11} &= \frac{\cos(y_\Psi)y_\rho}{\bar{y}_\rho} & m_{21} &= \frac{\sin(y_\Psi)y_\rho}{\bar{y}_\rho} \\ m_{12} &= -\sin(y_\Psi)\bar{y}_\rho & m_{22} &= \cos(y_\Psi)\bar{y}_\rho \\ m_{13} &= -\frac{\cos(y_\Psi)y_{\text{alt}}}{\bar{y}_\rho} & m_{23} &= -\frac{\sin(y_\Psi)y_{\text{alt}}}{\bar{y}_\rho}, \end{aligned}$$

is the mapping Jacobian matrix from cylindrical coordinates to the debiased Cartesian position given by (20).

4 The navigation system

When relying on only a single PARS antenna for position measurements, blocking of the signal path, resulting in measurement dropout, and the multipath discussed in Section 3.1, resulting in outlier measurements, can be critical. This motivates the use of an INS aided by PARS, providing smoother position estimates, enabling detection and removal of outliers, and ability to navigate in the gaps between PARS measurements, if they are short. The INS also provides estimates of the velocity and attitude of the UAV at high sampling rates, which is needed for feedback in the autopilot controllers. While this article seeks to give a practical overview of the navigation system, and includes the central equations for completeness, the full derivation can be found in (Gryte, 2020).

The MEKF, which is the key algorithm in the navigation system, consists of several parts, see Figure 2. The inertial navigation system, mimic the kinematic of the vehicle by integrating the inertial measurements, specific force and angular rate, using the strapdown equations (6), running synchronously with the IMU measurements that are assumed to arrive at with precise timestamps. To account for the drift of the inertial sensors, the navigation system relies on an aiding position measurement, which in this case is PARS-based.

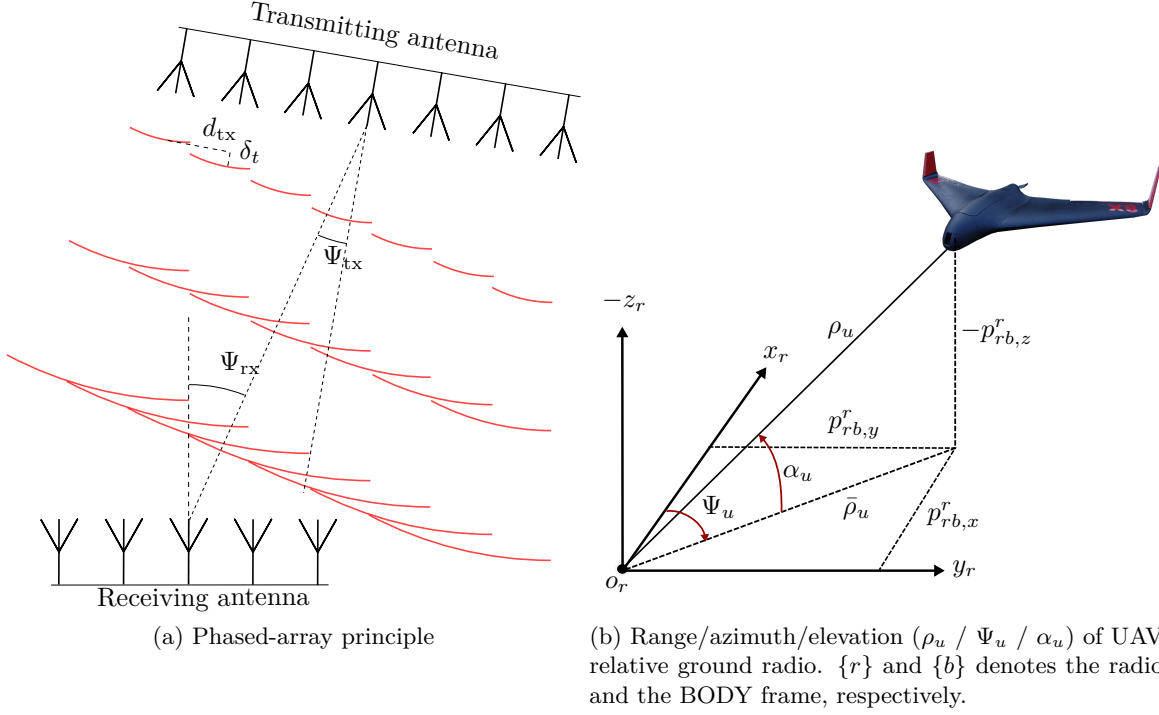


Figure 1: Phased-array radio navigation

For the presented INS, this aiding relies on indirect feedback from a multiplicative extended Kalman filter, which steer the INS state $\mathbf{x}_{\text{ins}} = (\mathbf{p}_{nb,\text{ins}}^n; \mathbf{v}_{nb,\text{ins}}^n; \mathbf{q}_{b,\text{ins}}^n; \mathbf{b}_{\text{acc},\text{ins}}^b; \mathbf{b}_{\text{ars},\text{ins}}^b)$ to the true state

$$\mathbf{x}_{\text{ins}} \rightarrow \mathbf{x} \quad (25)$$

when the error state goes to zero (or the identity quaternion), where the MEKF error state $\delta \mathbf{x} = (\delta \mathbf{p}; \delta \mathbf{v}; \delta \mathbf{a}; \delta \mathbf{b}_{\text{acc}}; \delta \mathbf{b}_{\text{ars}})$, and its model is derived from the true state, \mathbf{x} , based on

$$\mathbf{x} = \mathbf{x}_{\text{ins}} \oplus \delta \mathbf{x}, \quad (26)$$

where \oplus represents the $+$ or the \otimes operator, depending on whether the given INS error state is additive or multiplicative. The attitude error is represented using the four times Modified Rodrigues Parameters (MRP), whose relation to the quaternion is given by

$$\delta \mathbf{a} = 4\delta \mathbf{a}_{\text{mrp}} = 4 \frac{\delta \mathbf{q}_v}{1 + \delta q_s} \quad (27)$$

as given in (Markley, 2003). As seen in Figure 2, the update from the aiding measurements may be run asynchronously.

4.1 INS

By mimicking the kinematics in Section 2.4 the kinematic model

$$\dot{\mathbf{p}}_{nb,\text{ins}}^n = \mathbf{v}_{nb,\text{ins}}^n \quad (28)$$

$$\dot{\mathbf{v}}_{nb,\text{ins}}^n = \mathbf{R}_{nb}(\mathbf{q}_{b,\text{ins}}^n) \hat{\mathbf{f}}_{nb}^b + \mathbf{g}_b^n \quad (29)$$

$$\dot{\mathbf{q}}_{b,\text{ins}}^n = \frac{1}{2} \boldsymbol{\Omega}(\hat{\boldsymbol{\omega}}_{nb}^b) \mathbf{q}_{b,\text{ins}}^n, \quad (30)$$

and the bias model

$$\dot{\mathbf{b}}_{\text{acc,ins}}^b = -\mathbf{T}_{\text{acc}}^{-1} \mathbf{b}_{\text{acc,ins}}^b \quad (31)$$

$$\dot{\mathbf{b}}_{\text{ars,ins}}^b = -\mathbf{T}_{\text{ars}}^{-1} \mathbf{b}_{\text{ars,ins}}^b \quad (32)$$

are obtained, where

$$\hat{\mathbf{f}}_{nb}^b := \mathbf{f}_{\text{imu}}^b - \mathbf{b}_{\text{acc,ins}}^b, \quad \hat{\boldsymbol{\omega}}_{nb}^b := \boldsymbol{\omega}_{\text{ars}}^b - \mathbf{b}_{\text{ars,ins}}^b, \quad (33)$$

in which the IMU measurements are modeled as

$$\mathbf{f}_{\text{imu}}^b = \mathbf{f}_{nb}^b + \mathbf{b}_{\text{acc}}^b + \boldsymbol{\varepsilon}_{\text{acc}}^b, \quad (34)$$

$$\boldsymbol{\omega}_{\text{imu}}^b = \boldsymbol{\omega}_{nb}^b + \mathbf{b}_{\text{ars}}^b + \boldsymbol{\varepsilon}_{\text{ars}}^b, \quad (35)$$

and where $\mathbf{T}_{\text{acc}} = T_{\text{acc}} \cdot \mathbf{I}_3$ and $\mathbf{T}_{\text{ars}} = T_{\text{ars}} \cdot \mathbf{I}_3$ are the time constants for the Gauss-Markov model for the accelerometer (ACC) and angular rate sensor (ARS) biases, respectively. Being an error state Kalman filter, the state is integrated directly using (28) to (32), which also are important in the covariance update. Together with (26), it is possible to arrive at a set of differential equations for the error state, see (Gryte, 2020, Appendix B). These equations are then linearized to arrive at the linear, time-varying model

$$\delta \dot{\mathbf{x}} = \mathbf{A}(t) \delta \mathbf{x} + \mathbf{B}(t) \boldsymbol{\varepsilon}, \quad (36)$$

$$\boldsymbol{\varepsilon} = (\boldsymbol{\varepsilon}_{\text{acc}}^b; \boldsymbol{\varepsilon}_{\text{ars}}^b; \boldsymbol{\varepsilon}_{b,\text{acc}}^b; \boldsymbol{\varepsilon}_{b,\text{ars}}^b), \quad (37)$$

where the process noise form the spectral density matrix $\mathbf{Q}(t)$ according to

$$\mathbb{E}[\boldsymbol{\varepsilon}(t) \boldsymbol{\varepsilon}^\top(t - \tau)] = \mathbf{Q}(t) \delta(t - \tau). \quad (38)$$

The system matrix $\mathbf{A}(t)$ is then discretized using a first order approximation

$$\mathbf{A}_d[k] = \mathbf{I}_{15} + T_s \mathbf{A}(t), \quad (39)$$

while the process noise spectral density matrix is first mapped from the input space into the state space, through a similarity transform using $\mathbf{B}(t)$, before it is discretized to the covariance matrix $\mathbf{Q}_d[k]$ according to

$$\mathbf{Q}_d[k] = \int_0^{T_s} \mathbf{A}_d[k] \mathbf{B}(\tau) \mathbf{Q}(\tau) \mathbf{B}^\top(\tau) \mathbf{A}_d^\top[k] d\tau, \quad (40)$$

The discrete state transition matrix \mathbf{A}_d and the process covariance matrix \mathbf{Q}_d , are needed to propagate the state covariance

$$\mathcal{P}^-[k+1] = \mathbf{A}_d[k] \mathcal{P}^+[k] \mathbf{A}_d^\top[k] + \mathbf{Q}_d[k], \quad (41)$$

where \mathcal{P}^- and \mathcal{P}^+ indicate the a-priori and a-posteriori state covariance matrices, respectively.

4.2 Aiding measurement

Pure integration of (28) to (32) leads to drifting state estimates, due to the bias and noise found in inertial sensors. The INS thus relies on aiding from other sensors to correct itself. Aiding can also be used to inject information, such as knowledge that the aircraft is are stationary before takeoff, to improve the INS convergence.

4.2.1 PARS and altitude

As a result of obtaining a Cartesian position measurement with the transforms (20) to (21), the measurement \mathbf{y} is obtained from (21) directly, where it is assumed that the exogenous altitude measurements are sampled at such a high frequency that the PARS and altitude measurements can be assumed to be simultaneous. The measurement matrix becomes

$$\mathbf{C} = (\mathbf{I}_3 \quad \mathbf{0}_{3 \times 3} \quad \mathbf{0}_{3 \times 3} \quad \mathbf{0}_{3 \times 3} \quad \mathbf{0}_{3 \times 3}). \quad (42)$$

The covariance matrix \mathcal{R} is given in (22), while the predicted measurement trivially becomes

$$\hat{\mathbf{y}} = \mathbf{p}_{nb,ins}^n. \quad (43)$$

4.2.2 Altitude

In the event of a single altitude measurement, without a PARS measurement, the measurement equation is given by (14), while the measurement matrix becomes

$$\mathbf{C} = (\mathbf{1}_3 \quad \mathbf{0}_{3 \times 3} \quad \mathbf{0}_{3 \times 3} \quad \mathbf{0}_{3 \times 3} \quad \mathbf{0}_{3 \times 3}), \quad (44)$$

where $\mathbf{1}_3 = \text{diag}(0, 0, 1)$. The covariance matrix

$$\mathcal{R} = \sigma_{\text{alt}}^2, \quad (45)$$

is a single, tunable parameter, while the predicted measurement trivially becomes

$$\hat{y} = p_{nb,z}^n. \quad (46)$$

4.2.3 Pre-launch calibration

Accelerometer leveling is used to exploit information about the UAV being at rest, with the goal of initializing the roll and pitch angles. (7) can then be simplified to

$$\mathbf{f}_{\text{imu}}^b \approx -\mathbf{R}_{nb}^\top \mathbf{g}_b^n + \mathbf{b}_{\text{acc}}^b + \boldsymbol{\varepsilon}_{\text{acc}}, \quad (47)$$

since it is known that the linear and angular velocities are zero. This result in

$$\mathbf{y}_{\text{acc}} = \mathbf{f}_{\text{imu}}^b, \quad (48)$$

$$\hat{\mathbf{y}}_{\text{acc}} = -\mathbf{R}_{nb,ins}^\top \mathbf{g}_b^n + \mathbf{b}_{\text{acc},ins}^b, \quad (49)$$

$$\mathbf{C}_{\text{acc}} = \begin{pmatrix} \mathbf{0}_{3 \times 3} & \mathbf{0}_{3 \times 3} & -\mathbf{S}(\mathbf{R}_{nb,ins}^\top \mathbf{g}_b^n) & \mathbf{I}_3 & \mathbf{0}_{3 \times 3} \end{pmatrix}, \quad (50)$$

The 3×3 covariance matrix

$$\mathcal{R}_{\text{acc}} = \sigma_{\text{acc}}^2 \cdot \mathbf{I}_3 \approx \mathcal{Q}_{\text{acc}}/T_s, \quad (51)$$

is given by the covariance of the accelerometer measurements. Since it is also known that the UAV has zero angular velocity pre-launch, this can be utilized to estimate the ARS bias, since the ARS only measures the ARS bias and noise. Hence,

$$\mathbf{y}_{\text{ars}} = \boldsymbol{\omega}_{\text{imu}}^b, \quad (52)$$

$$\hat{\mathbf{y}}_{\text{ars}} = \mathbf{b}_{\text{ars},ins}^b, \quad (53)$$

$$\mathbf{C}_{\text{ars}} = (\mathbf{0}_{3 \times 3} \quad \mathbf{0}_{3 \times 3} \quad \mathbf{0}_{3 \times 3} \quad \mathbf{0}_{3 \times 3} \quad \mathbf{I}_3). \quad (54)$$

Again, the 3×3 covariance matrix

$$\mathcal{R}_{\text{ars}} = \sigma_{\text{ars}}^2 \cdot \mathbf{I}_3 \approx \mathcal{Q}_{\text{ars}}/T_s, \quad (55)$$

is given by the covariance of the ARS measurements. Similarly, it is known that the UAV is standing still, and thus have no linear velocity, which can be exploited by the virtual measurement and

$$\mathbf{y}_{\text{vel}} = \mathbf{0}, \quad (56)$$

$$\hat{\mathbf{y}}_{\text{vel}} = \mathbf{v}_{nb,\text{ins}}^n, \quad (57)$$

$$\mathbf{C}_{\text{vel}} = (\mathbf{0}_{3 \times 3} \quad \mathbf{I}_3 \quad \mathbf{0}_{3 \times 3} \quad \mathbf{0}_{3 \times 3} \quad \mathbf{0}_{3 \times 3}). \quad (58)$$

Under the assumption of standing perfectly still, the covariance matrix can be set very small, which will give faster convergence. For heading initialization, one can utilize a magnetometer, $\mathbf{y}_{\text{mag}} = \mathbf{m}_{nb}^b + \boldsymbol{\varepsilon}_{\text{mag}}$, with

$$\mathbf{C}_{\text{mag}} = (\mathbf{0}_{3 \times 3} \quad \mathbf{0}_{3 \times 3} \quad \mathbf{S}(\mathbf{R}_{nb,\text{ins}}^\top \mathbf{m}_{nb}^n) \quad \mathbf{0}_{3 \times 3} \quad \mathbf{0}_{3 \times 3}), \quad (59)$$

where \mathbf{m}_{nb}^b is the magnetic field in body frame.

4.3 Outlier rejection

To avoid degradation of the position, velocity and attitude estimates from bad PARS measurements, as discussed in Section 3, the reliability of the measurements is assessed by a test statistic, and possibly rejected in the event of an outlier.

Given the normalized residual (Gustafsson, 2012, Section 7.6.1)

$$\boldsymbol{\epsilon} = (\mathbf{C}\mathcal{P}^{-1}\mathbf{C}^\top + \mathcal{R})^{-\frac{1}{2}}(\mathbf{y} - \mathbf{C}\hat{\mathbf{x}}), \quad (60)$$

in which the central limit theorem motivates the Gaussian approximation, the null hypothesis of the measurement being an inlier, is discarded if the test statistic

$$T(\mathbf{y}_{\text{pars}}^r) = (\mathbf{R}_{nr}\mathbf{y}_{\text{pars}}^r - \mathbf{C}\mathbf{x}_{\text{ins}})^\top (\mathbf{C}\mathcal{P}^{-1}\mathbf{C}^\top + \mathcal{R})^{-1} (\mathbf{R}_{nr}\mathbf{y}_{\text{pars}}^r - \mathbf{C}\mathbf{x}_{\text{ins}}) \quad (61)$$

is above some limit χ_α^2 , corresponding to a χ -squared distribution with a confidence interval of $1 - \alpha$, which for the PARS measurements has three degrees of freedom.

4.4 Multiplicative extended Kalman filter (MEKF)

The measurement \mathbf{y} , prediction $\hat{\mathbf{y}}$, measurement matrix \mathbf{C} and measurement covariance matrix \mathcal{R} , are formed from the available aiding measurement for the current time step using equations from Section 4.2. For the given error state vector, the MEKF then becomes

$$\mathbf{K}[k] = \mathcal{P}^{-1}[k]\mathbf{C}^\top[k] \left(\mathbf{C}[k]\mathcal{P}^{-1}[k]\mathbf{C}^\top[k] + \mathcal{R}[k] \right)^{-1}, \quad (62)$$

$$\delta\hat{\mathbf{x}}[k] = \mathbf{K}[k](\mathbf{y}[k] - \hat{\mathbf{y}}[k]), \quad (63)$$

$$\mathcal{P}^+[k] = (\mathbf{I}_n - \mathbf{K}[k]\mathbf{C}[k])\mathcal{P}^{-1}[k](\mathbf{I}_n - \mathbf{K}[k]\mathbf{C}[k])^\top + \mathbf{K}[k]\mathcal{R}[k]\mathbf{K}^\top[k], \quad (64)$$

where $n = 15$ is the size of the error state space. The INS states with a linear relationship to the corresponding error states, are updated according to

$$\mathbf{p}_{nb,\text{ins}}^n[k] = \mathbf{p}_{nb,\text{ins}}^n[k] + \delta\hat{\mathbf{p}}[k], \quad (65)$$

$$\mathbf{v}_{nb,\text{ins}}^n[k] = \mathbf{v}_{nb,\text{ins}}^n[k] + \delta\hat{\mathbf{v}}[k], \quad (66)$$

$$\mathbf{b}_{\text{acc,ins}}^b[k] = \mathbf{b}_{\text{acc,ins}}^b[k] + \delta\hat{\mathbf{b}}_{\text{acc}}[k], \quad (67)$$

$$\mathbf{b}_{\text{ars,ins}}^b[k] = \mathbf{b}_{\text{ars,ins}}^b[k] + \delta\hat{\mathbf{b}}_{\text{ars}}[k], \quad (68)$$

after every iteration of the MEKF, while the attitude is corrected using

$$\delta \mathbf{q}(\delta \hat{\mathbf{a}}[k]) = \frac{1}{16 + \delta \hat{\mathbf{a}}^\top[k] \delta \hat{\mathbf{a}}[k]} \begin{pmatrix} 16 - \delta \hat{\mathbf{a}}^\top[k] \delta \hat{\mathbf{a}}[k] \\ 8 \cdot \delta \hat{\mathbf{a}}[k] \end{pmatrix}, \quad (69)$$

$$\mathbf{q}_{b,\text{ins}}^n[k] = \mathbf{q}_{b,\text{ins}}^n[k] \otimes \delta \mathbf{q}(\delta \hat{\mathbf{a}}[k]). \quad (70)$$

similar to (Markley, 2003). If the attitude error ever exceeds $\pm 180^\circ$, which is nonphysical, the attitude error must be replaced with its shadow set (Markley and Crassidis, 2014) before applying (70). After the INS has been corrected for, the MEKF state and covariance is reset

$$\delta \hat{\mathbf{x}}[k] = \mathbf{0}_{n \times 1}, \quad (71)$$

$$\mathcal{P}^+[k] = \mathbf{G}(\delta \hat{\mathbf{u}}[k]) \cdot \mathcal{P}^+[k] \cdot \mathbf{G}^\top(\delta \hat{\mathbf{u}}[k]), \quad (72)$$

where \mathbf{G} depends on the attitude error. For the kinematics of the given parameterization, (69), it is given as

$$\mathbf{G}(\delta \hat{\mathbf{u}}[k]) = \begin{pmatrix} \mathbf{I}_6 & \mathbf{0}_{6 \times 3} & \mathbf{0}_{6 \times 3} \\ \mathbf{0}_{3 \times 6} & \delta \hat{q}_w \mathbf{I}_3 - \mathbf{S}(\delta \hat{q}_v) & \mathbf{0}_{6 \times 3} \\ \mathbf{0}_{6 \times 6} & \mathbf{0}_{6 \times 3} & \mathbf{I}_6 \end{pmatrix}. \quad (73)$$

5 System architecture and safety

To demonstrate the reliability of the presented navigation system in a BVLOS setting, a setup that ensures safe operation is required. BVLOS operations have strict requirements for risk management and airworthiness. This necessitates extended use of trusted and well-tested hardware and software solutions, allowing for few modifications. The ArduPlane autopilot software has been used extensively for BVLOS flights, both at our lab (Zolich et al., 2015) and by the ArduPlane community, it is desirable to build on top of this existing solution instead of modifying it, risking to introduce new bugs in safety-critical mechanisms. For this reason, the PARS-based navigation and guidance system is implemented in the DUNE unified navigation environment (Pinto et al., 2013) running on an onboard computer, a contained part of the payload. This is depicted in Figure 4, a simplified illustration of the different modules and how they are interconnected.

The ArduPlane subsystem runs independently of DUNE. Under normal operation, in any of the automatic modes in ArduPlane¹, the current desired waypoint is sent to the lateral L_1 guidance controller (Park et al., 2007) and the longitudinal total-energy based *TECS* controller. These guidance controllers are based on the state estimates from the navigation system in ArduPlane, which relies on measurements from a GNSS-based sensor suite. The desired roll and pitch angles from the guidance controllers are passed on to the low-level roll and pitch controller, respectively, while the throttle command is sent to the electronic speed controller.

Contrary, the DUNE subsystem relies on ArduPlane as an interface to the UAV, both in terms of actuation and for some navigation sensor data. Similarly to the Ardupilot subsystem, the current desired waypoint is sent to two LOS-based guidance controllers, see Section 5.2, that calculate the desired roll, pitch and throttle commands. These set points are then sent to the low-level ArduPlane controllers, through the Mavlink message *set attitude target* in GUIDED mode. Based on the quality of the GNSS-based state estimates from ArduPlane, the PARS-based state estimates from the presented navigation system, and input from the user, the navigation monitor selects which source is a viable candidate to provide the navigation state estimates to the rest of the DUNE subsystem, including the guidance controllers. In addition to the safety it provides, this switch simplifies the tuning process, as the guidance controllers can run based on estimates from both PARS- and GNSS-based navigation systems.

As the two navigation systems run in parallel, independent of each other, switching is seamless. This also implies that if any of the navigation systems should fail, it is possible to switch to the other system,

¹The automatic modes in ArduPlane are AUTO, LOITER, CIRCLE, GUIDED, LAND and return to launch (RTL)

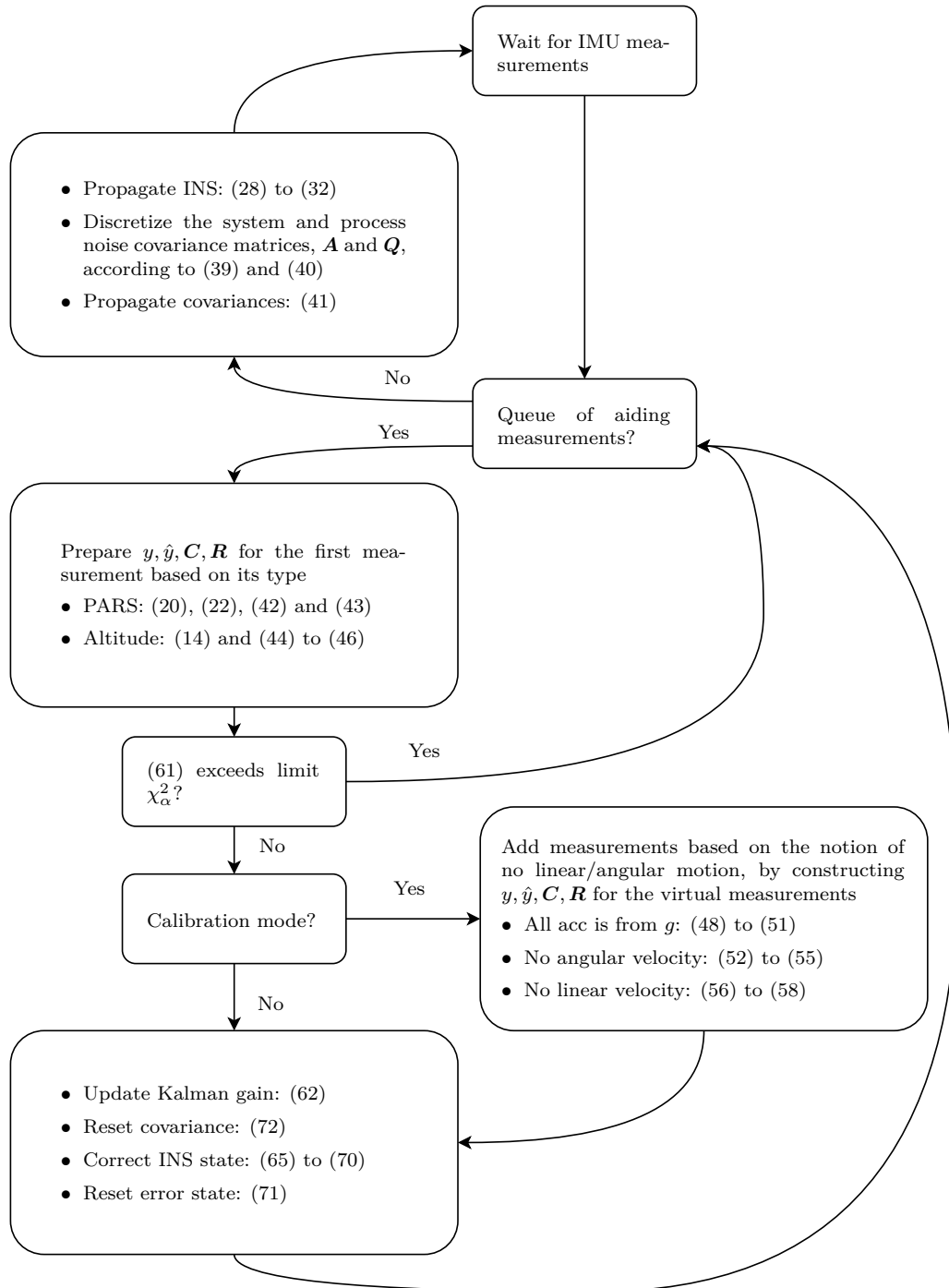


Figure 2: The different steps involved in the MEKF, and their accompanying equations

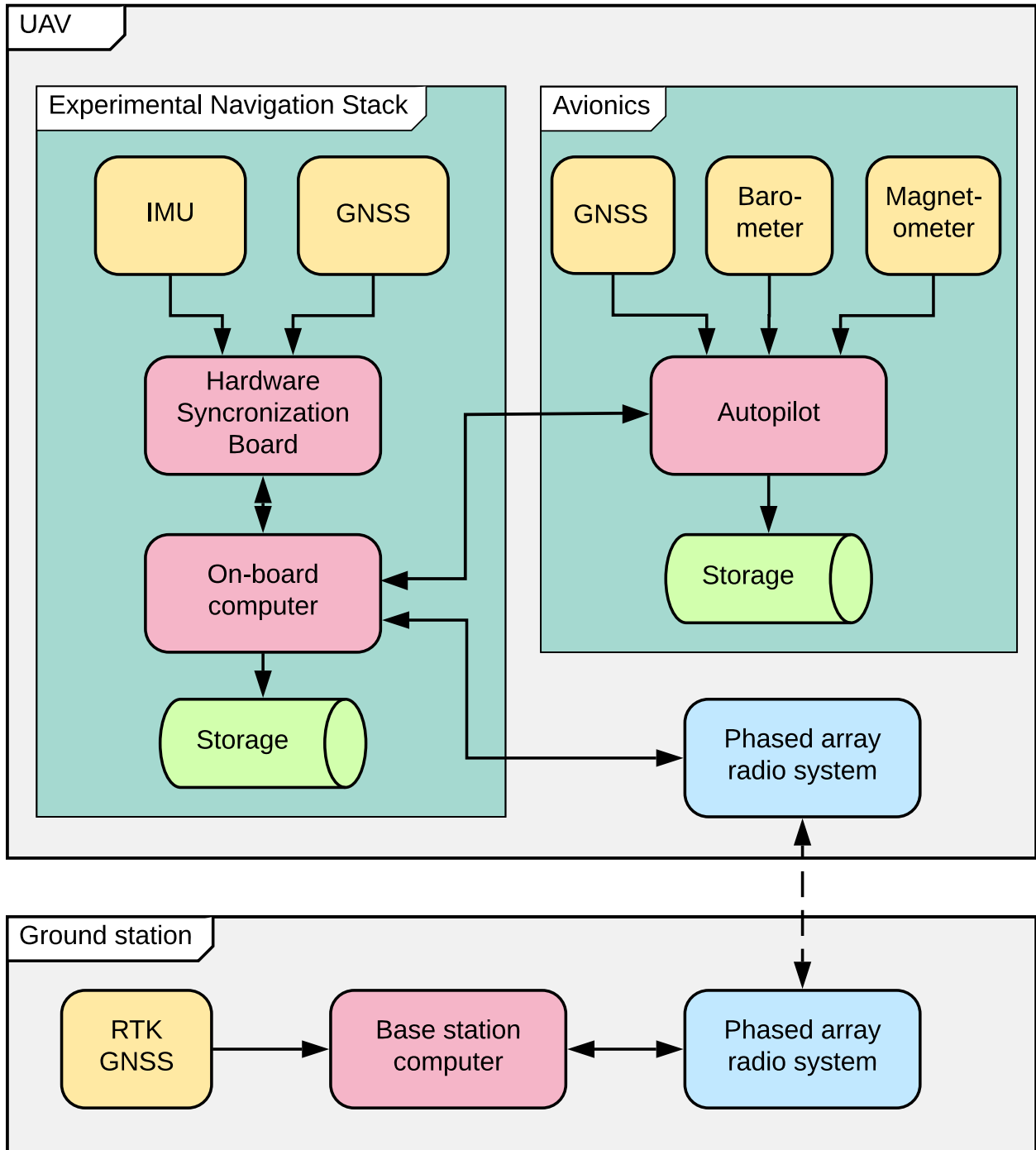


Figure 3: Overview of the PARS navigation stack and avionics. The UAV PARS position is calculated on the ground station, and is then transmitted to the UAV, over the PARS ethernet link. The barometer and magnetometer are internal to the autopilot, while the GPS is connected by UART. The autopilot connects to the onboard computer over a serial link. The IMU and second GNSS receiver are connected over serial links to the HW synchronization, which again is connected to the onboard computer over USB.

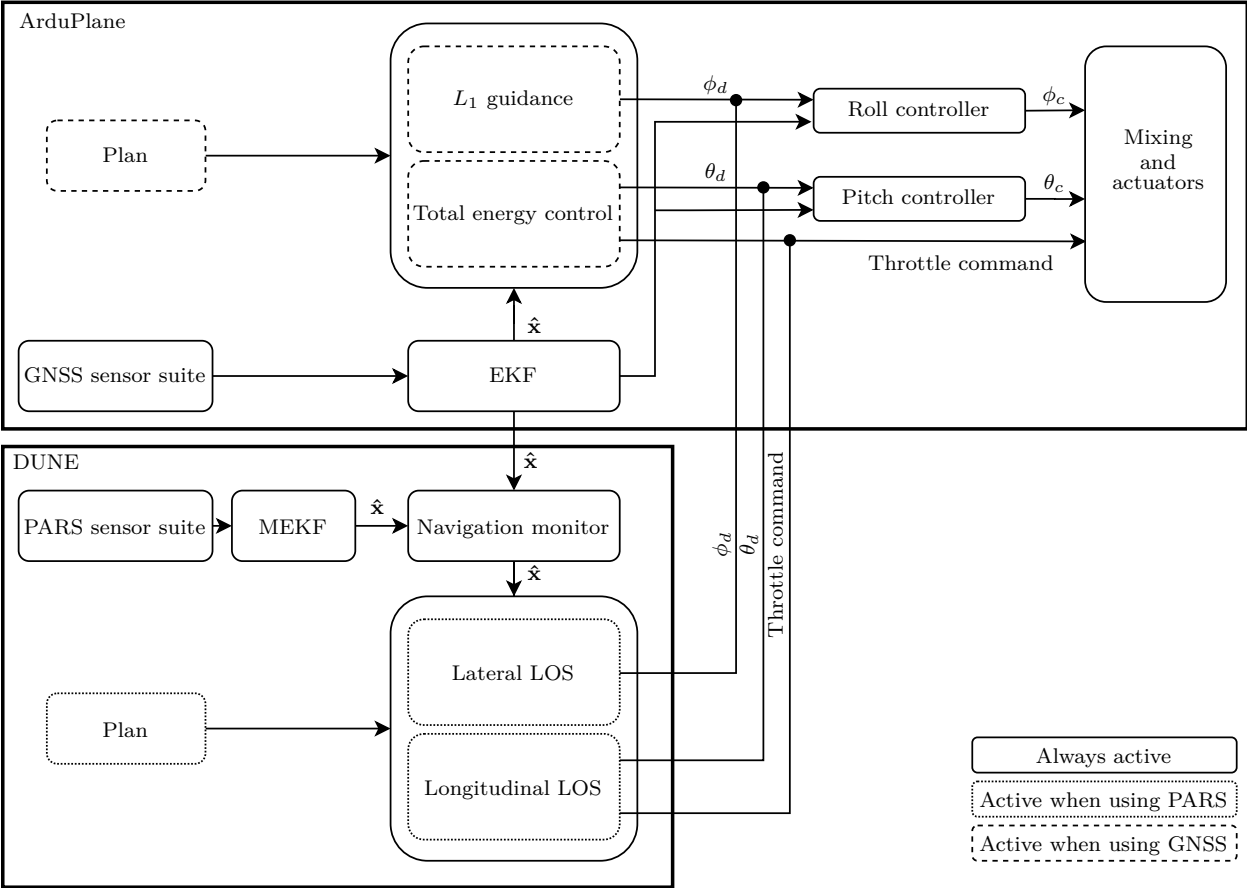


Figure 4: Block diagram of the interconnected system

which is assumed to be unaffected by the error that caused the first navigation system to fail. For these experiments, the system is focused on monitoring the state of the PARS-based estimates, but previous simulation studies (Albrektsen et al., 2018b) have shown the potential gains in robustness against GNSS radio frequency interference, when the nominally precise GNSS-based estimates are validated against the robust, but imprecise PARS-based estimates.

It should be noted that when using the PARS-based estimates along with the guidance controllers in DUNE, the system still depends on the pitch and roll estimates from the GNSS-based ArduPlane navigation system, as they are used to find the pitch and roll control errors. However, the roll and pitch estimates rely primarily on IMU measurements, and will likely be very similar to the roll and pitch estimates from the PARS-based INS. This is obviously only a simplification made from practical considerations, as there is no simple, non-intrusive way to get the low-level ArduPlane controllers to use the PARS-based estimates with the existing ArduPlane interface.

5.1 Safety mechanisms

In addition to switching between navigation sources, the navigation monitor also monitors the difference between the position and attitude estimates for the two navigation systems, and dispatches an abort message if the differences are large. The following abort triggers are considered

- Sudden large jumps in either position or attitude
- Loss of contact with the PARS base antenna
- Manual trigger, where the operator looked for trends in the estimates, such as small and persistent offsets in roll or pitch, which could cause stall or severe loss of lift

The abort message is consumed by an abort plan dispatcher, which will initiate a plan of user-configurable waypoints that are either stationary or relative to the current GNSS-based UAV position. As this is an AUTO-mode plan, it switches to navigate using the ArduPlane controllers and GNSS-based state estimates.

In the extreme scenario that contact with the ground station is lost, e.g. as a result of poor navigation, ArduPlane will trigger a failsafe and enter a **return-to-launch (RTL)** mode. Being a non-GUIDED mode, this again causes the ArduPlane GNSS navigation and controllers to guide the UAV back to the launch.

The mechanisms provide safe testing, by switching to GNSS when needed, while an operational system for use in GNSS-denied environments would be designed with opposite functionality, i.e. switch to PARS when GNSS is denied.

5.2 Guidance

Given the architecture described above, both lateral and longitudinal guidance controllers must be implemented in DUNE to calculate desired roll, pitch and throttle commands, based on the desired waypoints and on the current state of the UAV. The lateral controller implements line-of-sight path following based on (Gryte, 2020), which is derived from the coordinated turn relation, and is a generalization of the ArduPilot L_1 guidance. The desired roll angle is given by

$$\phi_d = \text{atan} \left(\frac{V_g \cos \gamma \cos \theta}{g \cos (\chi - \psi)} \left(K_1 \tilde{\chi} - \frac{\Delta}{\Delta^2 + y_e^2} \dot{y}_e + \dot{\chi}_p \right) - \sin \theta \tan (\chi - \psi) \right), \quad (74)$$

where y_e is the horizontal cross-track error, $\Delta = V_g \Delta_t$ is a user-configurable tuning variable that determines how far ahead along the path the UAV is aiming, V_g is the ground speed, γ is the flight path angle, χ_p



Figure 5: The four UAV antennas mounted in a diamond shape in the front part of the orange lid on the Skywalker X8, with the base antenna in the background

is the course angle of the path, $\tilde{\chi} = \chi_d - \chi$ is the error between the desired course $\chi_d = \chi_p + \text{atan}(\frac{-y_e}{\Delta})$ and the course χ . The lateral guidance law (74) renders the equilibrium $y_e = \tilde{\chi} = 0$ uniformly semiglobally exponentially stable.

The longitudinal guidance law is also based on LOS path following (You et al., 2012)

$$\gamma_d = \gamma_p + \text{atan} \left(\frac{K_{ph}z_e + K_{ih} \int z_e d\tau}{\Delta_h} \right) \quad (75)$$

where K_{\bullet} are controller gains, and $\Delta_h = \sqrt{R_{\text{enc}}^2 - z_e^2}$ is the vertical lookahead distance, tuned from the enclosure radius R_{enc} (Fossen, 2011). The angle of the path in the vertical plane is denoted γ_p , while z_e is the vertical cross-track error. The desired pitch is then (Harkegard and Glad, 2000)

$$\theta_d = \gamma_d + \alpha_{\text{trim}} - K_{\gamma,p}\tilde{\gamma}, \quad (76)$$

where $\tilde{\gamma} = \gamma_p - \gamma$, α_{trim} is the angle of attack at trim condition, while $K_{\gamma,p} > -1$ is a controller gain.

The throttle command is a signal in the range 0 to 100 which is given by a PI control on the airspeed error $\tilde{V}_a = V_{a,d} - V_a$, with a height error feed forward term,

$$T = K_{V,p}\tilde{V}_a + K_{V,i} \int \tilde{V}_a d\tau + K_{V,FF}z_e + T_{t,\text{trim}}, \quad (77)$$

where K_{\bullet} are controller gains, and $T_{t,\text{trim}}$ is the trim throttle.

6 Field experiments

To test the GNC system, the INS, safety mechanisms and guidance controllers were implemented in DUNE, and loaded onto the onboard computer, which was placed in a Skywalker X8 fixed-wing UAV, see Figure 5. The hardware, based on the standard fixed-wing payload at the NTNU UAVlab (Zolich et al., 2015; Albrektsen et al., 2017; Gryte et al., 2019), is illustrated in Figure 3. The navigation payload consists of

- Pixhawk autopilot, running ArduPlane 4.0.0, with accompanying magnetometer, barometer and airspeed sensor.
- Radionor CRE-189 ground station PARS, with specifications given in Table 2, seen along with the UAV in Figure 5
- Radionor CRE2-144-LW UAV-side PARS, with specifications given in Table 2
- Odroid XU4 onboard computer running Ubuntu Server 19.04
- SenTiBoard sensor interface and hardware synchronization board
- Two Ublox ZED-F9 GNSS receivers, sharing the same antenna, configured for 10 Hz GPS L1C/A and L2C, GLONASS G1 and G2, Galileo E1B/C and E5b, and Beidou B11 and B21. One receiver is connected to the autopilot and another is connected to the SenTiBoard.
- Sensoror STIM300 IMU, providing specific force and angular rate measurements at 250 Hz

The PARS-based INS runs synchronously with the IMU measurements, while the aiding measurements are timestamped, added to a queue and processed sequentially as time allows. The time difference between the IMU measurements, as given by the SenTiBoard, determine the sample time for the INS. No compensation of time delays is made for the PARS measurement, as these are believed to be small compared to the measurement errors. Values for the tuning gains of the PARS-based INS are given in Table 3.

Table 1: Abort trigger limits

Parameter	Value
Max 4xMRP norm error	0.8 rad
Max NE norm error	100 m
Max NED norm error	100 m
Max pitch error	10°
Max roll error	10°
Trigger Minimum Time	3 s

Table 2: Specifications of the Radionor CRE2 system

Parameter	Value
RF bandwidth	14 MHz
Frequency range	C-band
Signal form	Proprietary

To avoid a single point of failure in the communication links, the telemetry is sent over two independent links: an ethernet link provided by the PARS radio, and a serial link provided by a 3DR 433 MHz radio, which is the standard radio for the Pixhawk. These links are then merged using Mavproxy on the ground station, and using the more lightweight Mavlink-router on the UAV side.

Values for the controller gains for the guidance controllers (74), (75) and (77) are given in Table 3. The lateral guidance controller is moderately tuned, to not make abrupt changes in the control signals in the event of jumps in the estimates. Both guidance controllers also include rate-limiting filters for the output reference angles, that are activated for jumps larger than 10° in roll and 5° in pitch, to avoid abrupt changes.

6.1 Dead-reckoning preliminary test

A series of tests were first performed to establish trust in the system, by testing the abort functionality, whose limits are seen in Table 1, and ultimately by testing how the system behaved in the worst-case scenario of losing contact between the aircraft and the ground station. To simulate this scenario, the program that calculates the spherical position from the PARS raw data was turned off, before being started again. This effectively disables the PARS measurements from reaching the INS, rendering it in a dead-reckoning situation, with only inertial and altitude measurements. The tests were performed at the Udduvoll airfield, near Trondheim, Norway, and consist of a simple 200 m by 100 m square.

The results are plotted in Figure 6, where the shaded area indicate that the PARS measurements are unavailable, while the vertical line at about 200 s, 120 s after the loss of PARS measurements, indicate that the NED position error between the PARS-based and GNSS-based estimates are more than 100 m, which

Table 3: Controller tuning

Parameter	Value	Parameter	Value
K_1	0.1	$K_{\gamma,p}$	0.2
Δ_t	6.0 s	$K_{V,p}$	5.0
Maximum Bank	35.0°	$K_{V,i}$	0.4
K_{ph}	0.006	$K_{V,FF}$	1.5
K_{ih}	0.05	α_{trim}	1°
R_{enc}	15.0 m	$T_{t,trim}$	65 –

Table 4: INS tuning values. The listed covariances, spectral densities and time constants, are to be interpreted as the diagonal value in a 3×3 matrix, such that the values apply for both the x, y and z axis

Parameter	Value	Parameter	Value
σ_Ψ	2°	α	0.05
σ_{alt}	5 m	$\mathcal{Q}_{b_{\text{acc}}}$	$4.150\,41 \times 10^{-6} \text{ m}^2/\text{s}^3$
σ_ρ	15 m	$\mathcal{Q}_{a_{\text{acc}}} = \sigma_{a_{\text{acc}}}^2$	$6.587\,78 \times 10^{-4} \text{ m}^2/\text{s}^5$
$P_p[0]$	100 m^2	$\mathcal{Q}_{b_{\text{ars}}}$	$3.950\,05 \times 10^{-15} \text{ rad}^2/\text{s}$
$P_v[0]$	$4 \text{ m}^2/\text{s}^2$	$\mathcal{Q}_{a_{\text{ars}}} = \sigma_{a_{\text{ars}}}^2$	$9.214\,68 \times 10^{-7} \text{ rad}^2/\text{s}^3$
$P_{b_{\text{acc}}}[0]$	$1 \text{ m}^2/\text{s}^4$	T_{acc}	3600 s
$P_{b_{\text{ars}}}[0]$	$3.046\,17 \times 10^{-6} \text{ rad}^2/\text{s}^2$	T_{ars}	3600 s
$P_a[0]$	$0.030\,461\,7 \text{ rad}^2$		

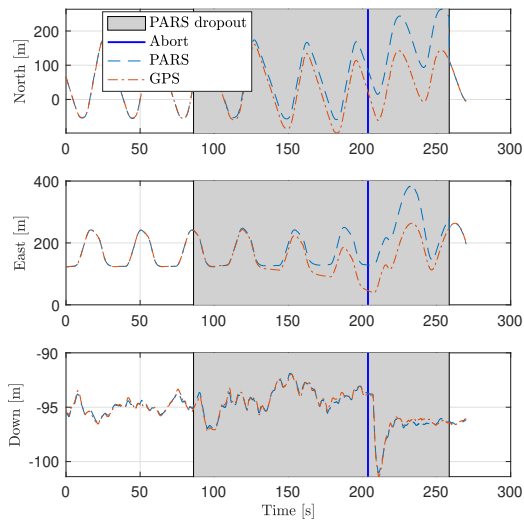
causes the abort plan to be triggered. As the abort plan differs from the previously flown plan, the response, particularly pitch, down position and down velocity, also changes. The PARS measurements are given in Figure 8 for reference.

As expected, Figures 6a and 7 shows that the horizontal position estimates of the INS drift when it is not aided by the PARS measurements. However, once the PARS measurements are available again, the position estimates quickly returns to the close vicinity of the GNSS-based estimates, about 260s into the experiment. Notice also that in the first part of the PARS dropout in Figure 6a, the guidance controllers seemingly keep the UAV in its desired path, which also is seen from Figure 7 where the PARS-based position estimates follow the same pattern as before the dropout. However, the GNSS-based position estimate, which is considered the ground truth in this case, shows that the pattern flown by the UAV is actually drifting eastward. While the attitude of the two navigation systems seem to follow each other closely in Figure 6c, the attitude error in Figure 6d, particularly the pitch, becomes slightly more noisy in the dead-reckoning. This might be due to the strong kinematic coupling between the attitude parameter and the vertical position component. Considering the NE estimation error velocities of Figure 6e, they also have the expected drift under dead-reckoning. This is not so apparent in the derived speed and course over ground, in Figure 6f, but the accompanying course error undoubtedly grows. The characteristics of all the estimation errors clearly change after the abort is triggered, as the flown path differs.

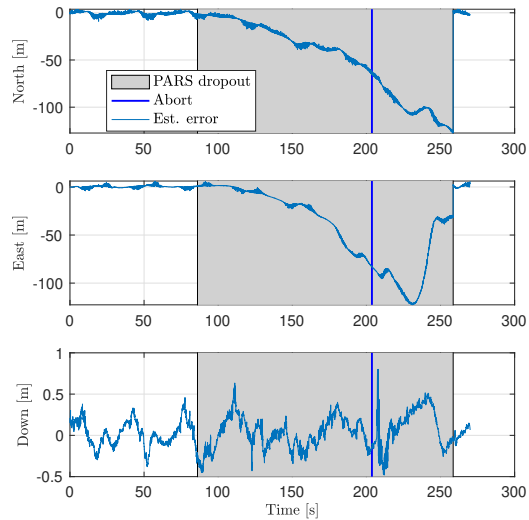
6.2 Navigation source switch preliminary test

To establish how the control performance is affected by the use of PARS-based navigation, compared to GNSS-based navigation, and during the switch between the two, another flight test was performed in the same location and with the same flight pattern as in Section 6.1. After flying one lap using the GNSS-based estimates, the switch was made to the PARS-based navigation system, indicated by the solid, horizontal line in Figure 9, which also shows the cross-track error, roll angle, desired roll angle, yaw angle and course angle. The cross-track error is qualitatively similar before and after the switch. However, as the estimates from the two navigation systems differ, the jump of about 1 m in cross-track error and 2° in yaw and course, seen in Figure 9b, is inevitable. These jumps are propagated through the guidance system, leading to a minor jump of 2° in the desired roll angle. This jump is within the allowable limits for the UAV, and is therefore not smoothed. As there are no integral terms in the lateral guidance controller, the jumps will not cause integral windup. It is interesting to note that after the switch, the roll angle seems to have a slightly higher value compared to before the switch. This is likely caused by the misalignments between the two navigation systems, as seen in Figures 6b and 7, but could also be affected by the fact that the low-level ArduPlane roll controller compares the PARS-based desired roll angle with the roll angle from the GNSS-based navigation system.

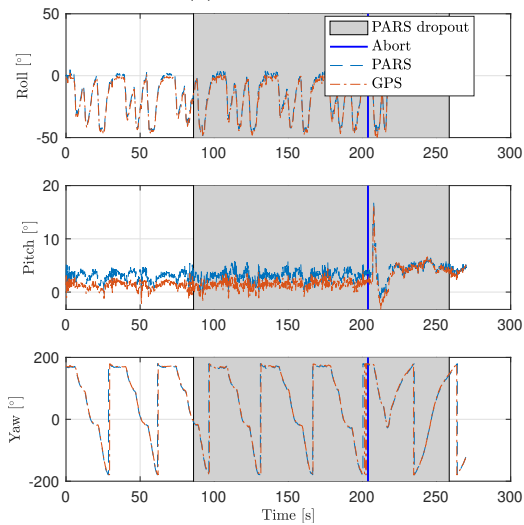
The longitudinal response to the navigation system switch is plotted in Figure 10, and shows the same tendency as for the lateral response in that the pitch after the switch is offset from the pitch before the



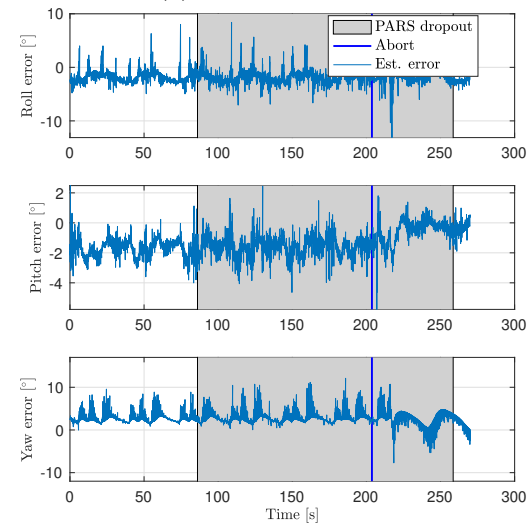
(a) NED position



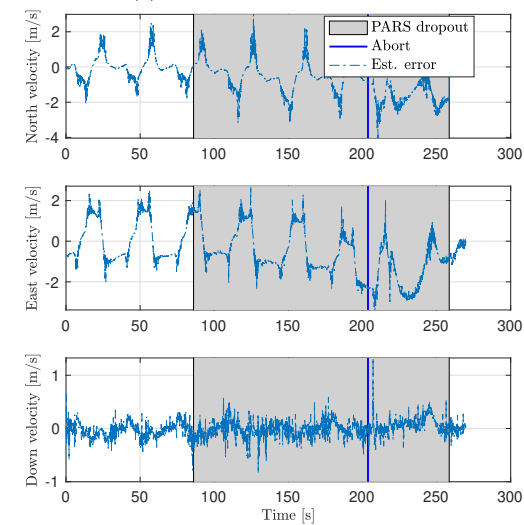
(b) NED position error



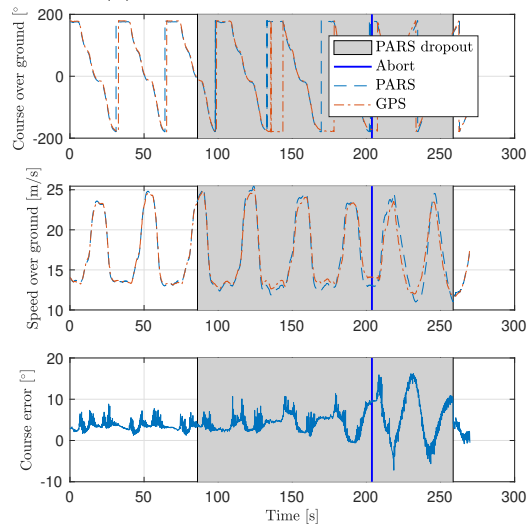
(c) Attitude in Euler angles



(d) Attitude error in Euler angles



(e) NED velocity errors



(f) Speed and course over ground

Figure 6: Dead-reckoning test

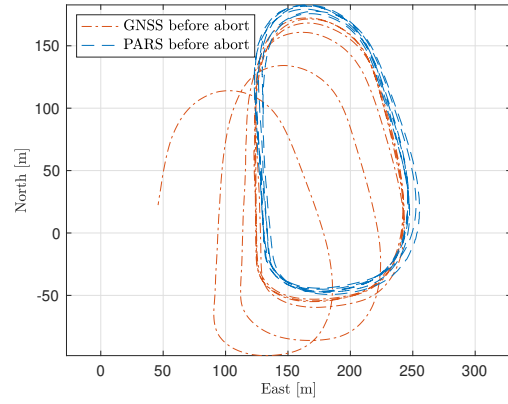


Figure 7: 2D NED position. The data after the abort plan is started are not shown, for clarity.

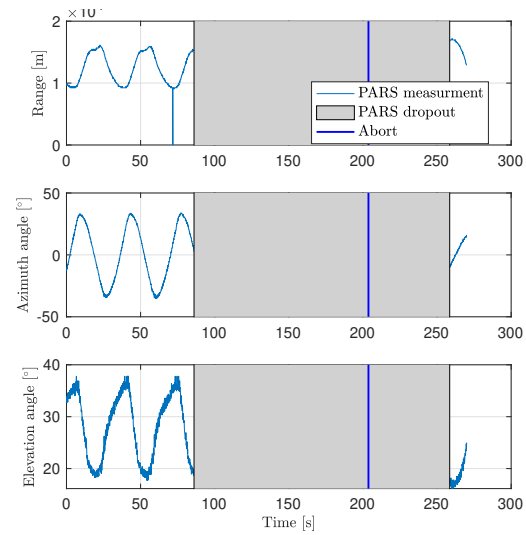


Figure 8: PARS measurements, dead-reckoning test

switch. There are integral terms in the longitudinal guidance controllers, that could potentially lead to integral windup in the switching, but this does not seem to be a problem in the data, as the difference between the height estimates of the two navigation systems is small.

When considering these results, it is important to keep in mind that the controller considers whatever navigation state it receives from the navigation monitor to be true. The cross-track error, and the derived output values, are functions of this navigation state, not the true position of the UAV. The uncertainty of the navigation system must also be considered to find the error between the true position of the UAV and the desired path, but this can be evaluated separately from the guidance controllers.

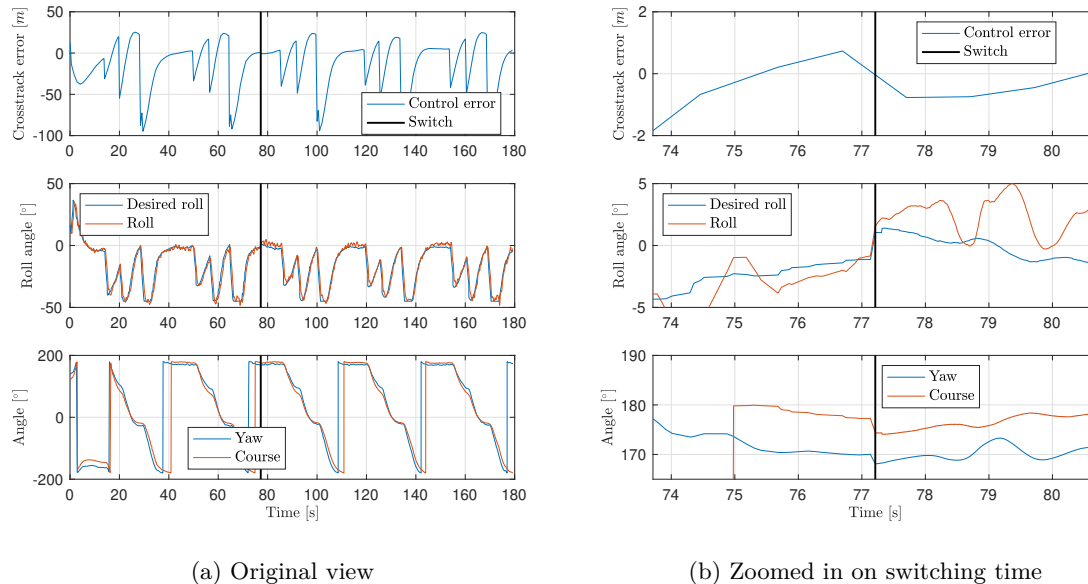


Figure 9: Lateral response from switching navigation source

6.3 BVLOS flight

To test the presented guidance and navigation system, a more extensive BVLOS flight in class D controlled airspace was performed at Raudstein, 45 km north-west of Trondheim, Norway. The flight consisted of a 20 km long track in a lawnmower pattern, see Figure 12a, where the most distant waypoint was over 5 km away from the base antenna, located on the shore just east of the plot view. The flight starts near the origin, then moves along the lawnmower pattern, before returning back in a straight line. Qualitatively, the PARS-based position estimates follow the GNSS-based estimates well, albeit with error of up to 80 m in north and 40 m in east, see Figure 15, with mean error, mean absolute error, standard deviation and root mean square error given in Table 5. Here, the norm column of e.g. the mean absolute error corresponds to the mean absolute error of the norm of the north/east/down components, as opposed to the norm of the mean absolute error of the north, east and down time series.

It is clear that the error in the down axis is small, for both position in Figure 15 and Table 5, and velocity in Figure 12d and Table 6, as the PARS-INS uses the exogenous altitude measurement. The altitude error undoubtedly grows with the geometric range, seen in Figure 15, which likely is an effect of the simplification of representing the altitude measurements in NED, when in reality the altitude is given as the WGS-84 ellipsoidal height difference between the current location and the base antenna. As the flight is about 5 km due east, this is expected to cause a height error of up to 2 m that is increasing with distance from the base, which is well aligned with the experienced height error in Figure 15. Figure 11 confirms that also the horizontal position estimation error increase with range, as expected given the angular uncertainty. The

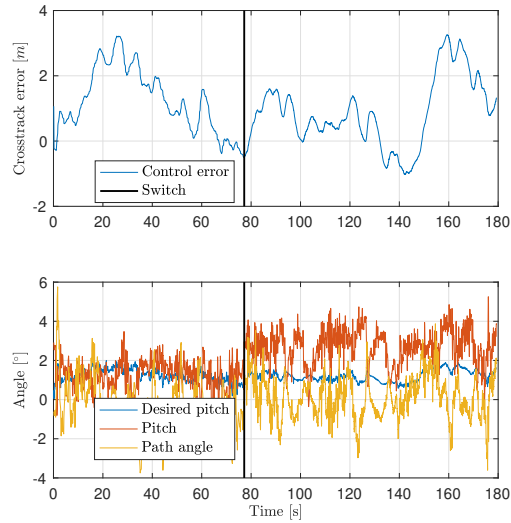


Figure 10: Longitudinal response from switching navigation source

error in the course over ground in Figure 12e, which is critical for the horizontal guidance controller, remains small throughout the experiment.

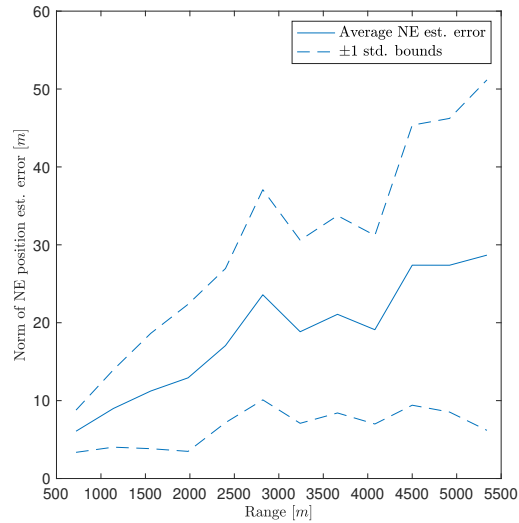


Figure 11: Bin average horizontal position estimation error, with standard deviation bounds, versus geometric range, for 12 bins.

The raw PARS geometric range, azimuth and elevation measurements are plotted in Figure 14, and show a handful of spikes in the measurements over the course of the flight. From the elevation angle it can also be seen when the PARS DoA algorithm jumps from one cluster of measurements to another which yields better communication, as discussed in Section 3. This is particularly visible at about 750 s, when the elevation angle jumps from about 10° to -20° . However, the effect of these spikes are not seen in the position estimates in Figures 12a and 15, as the measurements are rejected as outliers, and thus not considered by the INS.

While Figures 12b and 12c and Table 7 shows reasonable performance for roll and yaw, there is a slow drift

or convergence in the pitch estimate for one of the estimators. This could be caused by wrong initialization and slow convergence of the slowly varying ARS bias in the z-axis in the PARS-based navigation system, see Figure 13b, which affects the pitch estimate through

$$\dot{\theta} = \omega_{nb,y}^b \cos(\phi) - \omega_{nb,z}^b \sin(\phi), \quad (78)$$

and demonstrates that there is still some improvements to be made in the tuning. There is also some fluctuations in the accelerometer bias, particularly along the x-axis, seen in Figure 13a, which also indicate additional obtainable performance gains.

Table 5: PARS-INS NED position error statistics (versus GNSS-INS ground truth)

	North [m]	East [m]	Down [m]	Norm [m]
ME	13.46	10.76	0.8643	19.95
AME	15.35	11.05	0.8840	19.95
STD	16.38	7.601	0.6316	15.05
RMSE	21.20	13.17	1.071	24.99

Table 6: PARS-INS NED velocity error statistics (versus GNSS-INS ground truth)

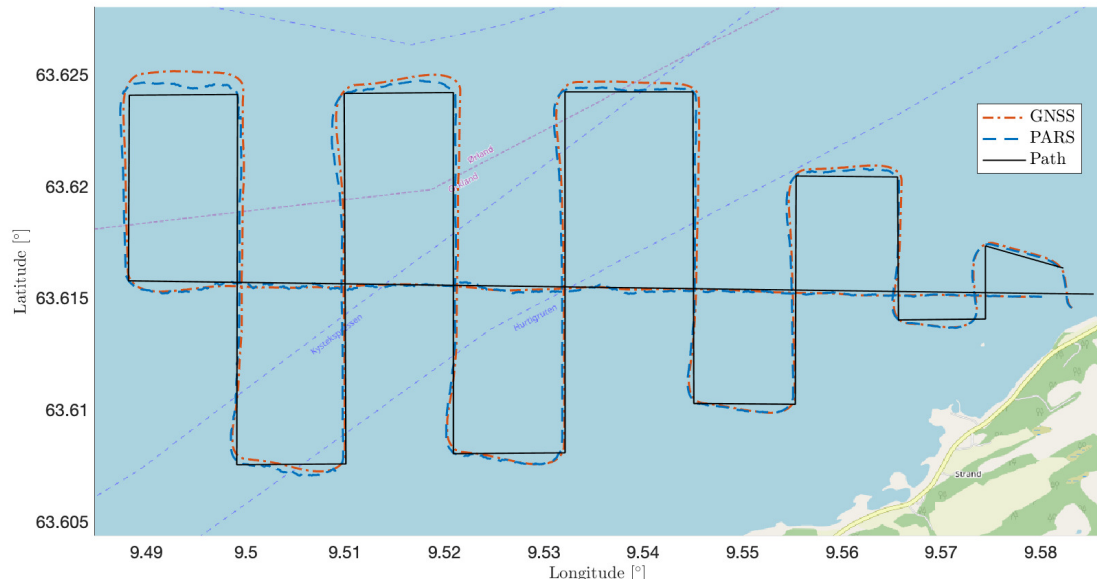
	North [m/s]	East [m/s]	Down [m/s]	Norm [m/s]
ME	0.1080	-0.06524	-0.008223	0.7884
AME	0.6648	0.2737	0.1212	0.7884
STD	0.8228	0.3777	0.1612	0.4899
RMSE	0.8298	0.3833	0.1614	0.9282

Table 7: PARS-INS attitude error statistics (versus GNSS-INS ground truth)

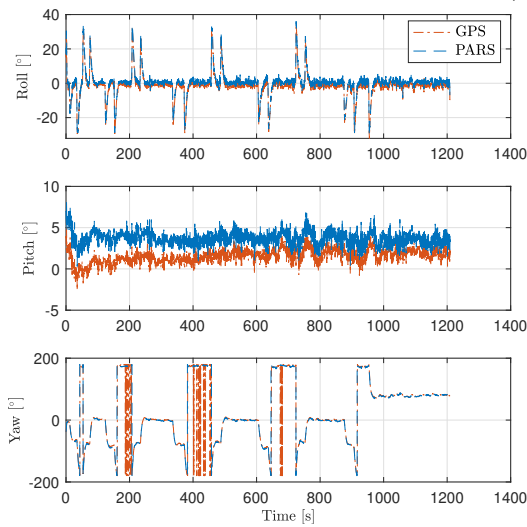
	Roll [°]	Pitch [°]	Yaw [°]	Norm [°]
ME	-1.675	-2.130	1.949	3.661
AME	1.743	2.133	2.021	3.661
STD	0.9815	0.7837	1.429	1.165
RMSE	1.941	2.270	2.417	3.842

7 Discussion

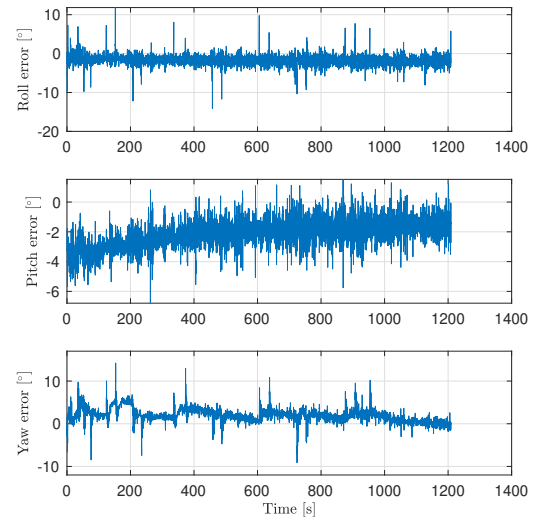
The results show that the PARS-aided navigation system has merit for autopilot flight control, although the position errors are larger than what one can expect from GNSS-based systems. When considering this, it is important to note the potential misalignment of the ground station PARS antenna. The antenna is manually calibrated by leveling the roll and pitch angles of the antenna, before the azimuth angle is measured using a compass. As the compass is susceptible to magnetic anomalies, this is validated in a comparison of the GNSS-based and PARS-based position estimates while the UAV is stationary on the ground, where the azimuth angle is adjusted until the positions align. When flying at ranges of over 5 km, a misalignment of 1° in azimuth, which is an optimistic scenario given the above calibration routine, alone leads to horizontal position errors just short of 100 m. The non-zero-mean position error in Figure 15 also supports this argument. This motivates further research into an additional calibration mode, that utilize GNSS measurements when available/allowable, to estimate the misalignment bias of the ground station PARS antenna. As the measurement covariance matrix, (22), is also affected by the misalignment in the mapping from $\{r\}$ to $\{n\}$, considering Θ_{PARS} a stochastic variable, with an uncertainty, could further improve the consistency of the filter. The performance of the guidance controllers are marginally affected by the use of PARS-based navigation estimates. The only qualitative differences in the performance can be attributed to misalignments in the two navigation systems, and to the current interconnection of the GNC system, where the PARS-based roll and pitch references are compared to the GNSS-based roll and pitch estimates.



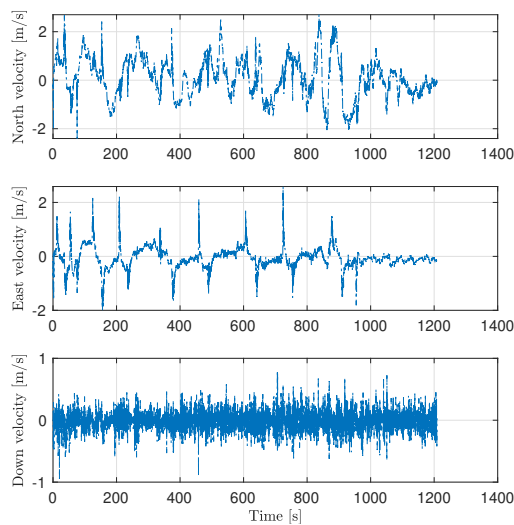
(a) Position



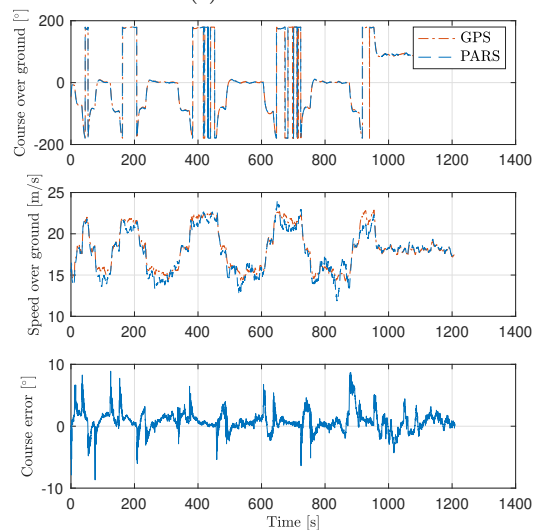
(b) Attitude



(c) Attitude error



(d) NED velocity error



(e) Speed and course over ground

Figure 12: Beyond-visual-line-of-sight experiment

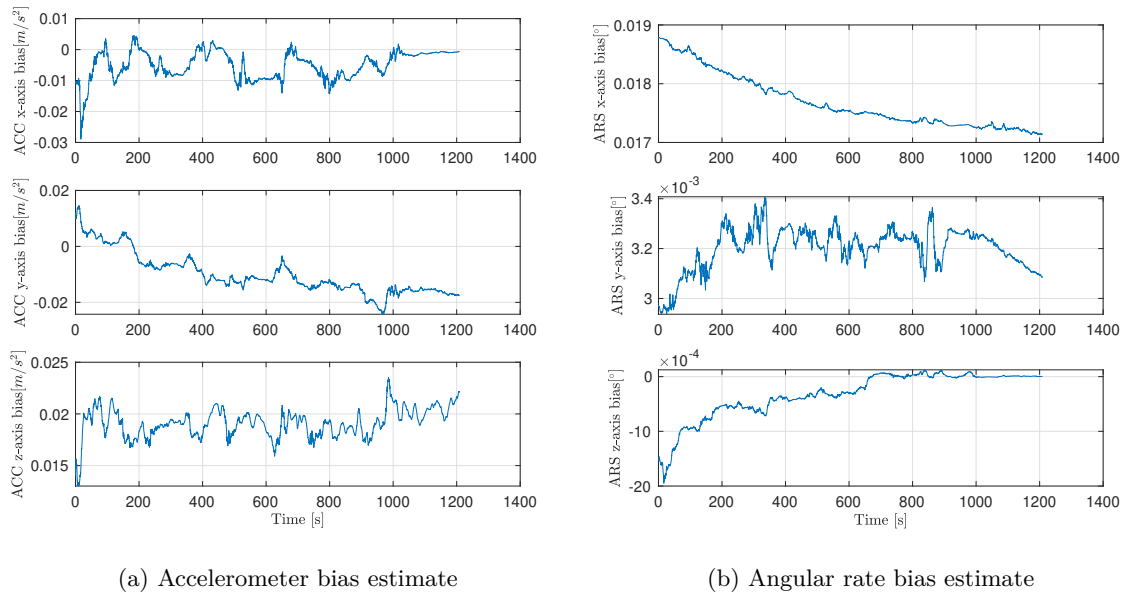


Figure 13: Estimated IMU biases, BVLOS experiment

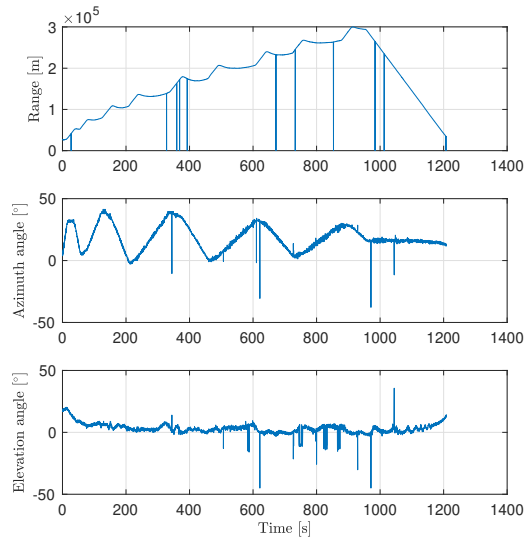


Figure 14: PARS measurements, BVLOS experiment

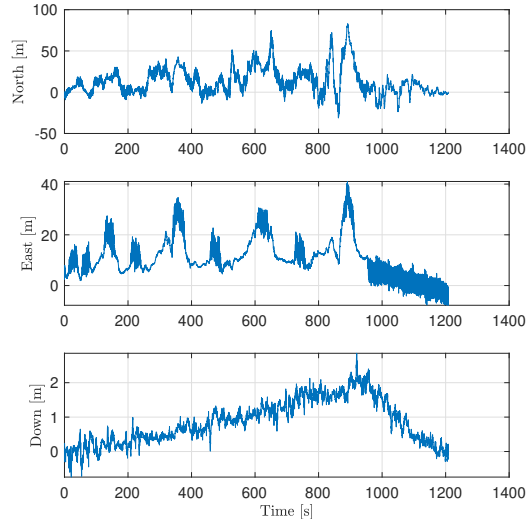


Figure 15: NED position error

8 Conclusion

The safety and accuracy of a GNSS-free flight control system has been demonstrated through field experiments involving beyond-visual-line-of-sight flight with a fixed-wing UAV over water. The navigation system relies on position measurements from a phased-array radio system, in addition to an exogenous altitude measurement, for a multiplicative extended Kalman filter to aid inertial measurements, without relying on a compass or magnetometer for heading measurement. Although the position errors, 19.95 m in the norm, are larger than what would have been expected with a similar GNSS-based system, a portion can likely be attributed to the misalignment of the phased-array ground station antenna. To safely operate the UAV, a system consisting of a guidance controller module and several safety mechanisms, like switching between and monitoring the different navigation systems, was designed and implemented.

Acknowledgments

The authors thanks Pål Kvaløy piloting the fixed-wing UAV, and Radionor Communications for technical support. This work was partly supported by the Norwegian Research Council and through the Hybrid Operations in Maritime Environments program at MAROFF together with the FRINATEK project Multi-stage global sensor fusion for navigation using nonlinear observers and eXogenous Kalman filter, the Center of Autonomous Marine Operations and Systems (NTNU AMOS) at the Norwegian University of Science and Technology (NTNU) and the H2020 ECSEL project Safe Cooperating Cyber-Physical System using Wireless Communication (SafeCOP) (grants no. 269480, 250725, 223254 and 692529-2, respectively).

References

- Abeida, H., Zhang, Q., Li, J., and Merabtine, N. (2013). Iterative sparse asymptotic minimum variance based approaches for array processing. *IEEE Transactions on Signal Processing*, 61(4):933–944.
- Albrektsen, S. M., Bryne, T. H., and Johansen, T. A. (2018a). Phased array radio system aided inertial navigation for unmanned aerial vehicles. In *Proc. of the IEEE Aerospace Conference*, pages 1–11, Big Sky, MT, USA.
- Albrektsen, S. M., Bryne, T. H., and Johansen, T. A. (2018b). Robust and secure UAV navigation us-

- ing GNSS, phased-array radiosystem and inertial sensor fusion. In *2nd IEEE Conference on Control Technology and Applications*, pages 1338–1345, Copenhagen, Denmark.
- Albrektsen, S. M., Sjøegrov, A., and Johansen, T. A. (2017). Navigation of UAV using phased array radio. In *Workshop on Research, Education and Development of Unmanned Aerial Systems (RED UAS)*, pages 138–143, Linköping, Sweden.
- Bar-Shalom, Y., Willett, P. K., and Tian, X. (2011). *Tracking and Data Fusion: A Handbook of Algorithms*. YBS Publishing.
- Chung, P.-J., Viberg, M., and Yu, J. (2014). Chapter 14 - DOA estimation methods and algorithms. In Zoubir, A. M., Viberg, M., Chellappa, R., and Theodoridis, S., editors, *Academic Press Library in Signal Processing: Volume 3*, volume 3 of *Academic Press Library in Signal Processing*, pages 599 – 650. Elsevier.
- Djugash, J., Hamner, B., and Roth, S. (2009). Navigating with ranging radios: Five data sets with ground truth. *Journal of Field Robotics*, 26(9):689–695.
- Engel, J., Schöps, T., and Cremers, D. (2014). LSD-SLAM: Large-scale direct monocular SLAM. In *13th European Conference on Computer Vision ECCV*, pages 834–849, Zurich, Switzerland. Springer.
- Farrell, J. A. (2008). *Aided Navigation: GPS with High Rate Sensors*. McGraw Hill.
- Forster, C., Pizzoli, M., and Scaramuzza, D. (2014). SVO: Fast semi-direct monocular visual odometry. In *2014 IEEE international conference on robotics and automation (ICRA)*, pages 15–22, Hong Kong, China. IEEE.
- Fossen, T. I. (2011). *Handbook of marine craft hydrodynamics and motion control*. John Wiley & Sons.
- Gade, K. (2018). *Inertial Navigation – Theory and Applications*. PhD thesis, Norwegian University of Science and Technology (NTNU).
- Gezici, S., Tian, Z., Giannakis, G. B., Kobayashi, H., Molisch, A. F., Poor, H. V., and Sahinoglu, Z. (2005). Localization via ultra-wideband radios: a look at positioning aspects for future sensor networks. *IEEE signal processing magazine*, 22(4):70–84.
- Gryte, K. (2020). *Precision control of fixed-wing UAV and robust navigation in GNSS-denied environments*. PhD thesis, Norwegian University of Science and Technology (NTNU).
- Gryte, K., Bryne, T. H., Albrektsen, S. M., and Johansen, T. A. (2019). Field test results of GNSS-denied inertial navigation aided by phased-array radio systems for UAVs. In *2019 International Conference on Unmanned Aircraft Systems (ICUAS)*, pages 1398–1406.
- Gustafsson, F. (2010). Particle filter theory and practice with positioning applications. *IEEE Aerospace and Electronic Systems Magazine*, pages 53–82.
- Gustafsson, F. (2012). *Statistical sensor fusion*. Studentlitteratur, 2 edition.
- Haardt, M., Pesavento, M., Roemer, F., and Korso, M. N. E. (2014). Chapter 15 - subspace methods and exploitation of special array structures. In Zoubir, A. M., Viberg, M., Chellappa, R., and Theodoridis, S., editors, *Academic Press Library in Signal Processing*, volume 3 of *Academic Press Library in Signal Processing*, pages 651 – 717. Elsevier.
- Harkegard, O. and Glad, S. T. (2000). A backstepping design for flight path angle control. In *Proceedings of the 39th IEEE Conference on Decision and Control, 2000.*, volume 4, pages 3570–3575. IEEE.
- Hovstein, V. E., Sjøegrov, A., and Johansen, T. A. (2014). Experiences with coastal and maritime UAS BLOS operation with phased-array antenna digital payload data link. In *Proc. International Conference Unmanned Aircraft Systems (ICUAS)*, pages 262–266, Orlando, FL.

- Jaffe, G. and Erdbrink, T. (2011). Iran says it downed U.S. stealth drone; Pentagon acknowledges aircraft downing. *The Washington post*.
- Karasz, P. (2019). Europe billed Galileo as its answer to GPS. It’s been mostly down for days. *The New York Times*.
- Kerns, A. J., Shepard, D. P., Bhatti, J. A., and Humphreys, T. E. (2014). Unmanned aircraft capture and control via GPS spoofing. *Journal of Field Robotics*, 31(4):617–636.
- Khattak, S., Papachristos, C., and Alexis, K. (2019). Keyframe-based thermal-inertial odometry. *Journal of Field Robotics*.
- Krim, H. and Viberg, M. (1996). Two decades of array signal processing research: the parametric approach. *IEEE Signal Processing Magazine*, 13(4):67–94.
- Mahfouz, M. R., Zhang, C., Merkl, B. C., Kuhn, M. J., and Fathy, A. E. (2008). Investigation of high-accuracy indoor 3-D positioning using UWB technology. *IEEE Transactions on Microwave Theory and Techniques*, 56(6):1316–1330.
- Markley, F. L. (2003). Attitude error representation for kalman filtering. *Journal of Guidance, Control, and Dynamics*, 26(2):311–317.
- Markley, F. L. and Crassidis, J. L. (2014). *Fundamentals of Spacecraft Attitude Determination and Control*, volume 33 of *Space Technology Library*. Springer-Verlag New York, 1 edition.
- Maruyama, T., Kihira, K., and Miyashita, H. (2016). *Phased Arrays*, pages 1113–1162. Springer Singapore, Singapore.
- Mohta, K., Watterson, M., Mulgaonkar, Y., Liu, S., Qu, C., Makineni, A., Saulnier, K., Sun, K., Zhu, A., Delmerico, J., Karydis, K., Atanasov, N., Loianno, G., Scaramuzza, D., Daniilidis, K., Taylor, C. J., and Kumar, V. (2017). Fast, autonomous flight in GPS-denied and cluttered environments. *Journal of Field Robotics*, 35(1):101–120.
- Mourikis, A. I. and Roumeliotis, S. I. (2007). A multi-state constraint kalman filter for vision-aided inertial navigation. In *Proceedings IEEE International Conference on Robotics and Automation*, pages 3565–3572, Roma, Italy. IEEE.
- Mur-Artal, R., Montiel, J. M. M., and Tardos, J. D. (2015). ORB-SLAM: A versatile and accurate monocular SLAM system. *IEEE transactions on robotics*, 31(5):1147–1163.
- Park, S., Deyst, J., and How, J. P. (2007). Performance and lyapunov stability of a nonlinear path following guidance method. *Journal of Guidance, Control, and Dynamics*, 30(6):1718–1728.
- Pinker, A. and Smith, C. (1999). Vulnerability of the GPS signal to jamming. *GPS Solutions*, 3(2):19–27.
- Pinto, J., Dias, P. S., Martins, R., Fortuna, J., Marques, E., and Sousa, J. (2013). The LSTS toolchain for networked vehicle systems. In *OCEANS-Bergen, 2013 MTS/IEEE*, pages 1–9. IEEE.
- Roy, R. and Kailath, T. (1989). ESPRIT-estimation of signal parameters via rotational invariance techniques. *IEEE Transactions on Acoustics, Speech, and Signal Processing*, 37(7):984–995.
- Schmidt, D., Radke, K., Camtepe, S., Foo, E., and Ren, M. (2016). A survey and analysis of the GNSS spoofing threat and countermeasures. *ACM Computing Surveys (CSUR)*, 48(4):1–31.
- Schmidt, R. (1986). Multiple emitter location and signal parameter estimation. *IEEE Transactions on Antennas and Propagation*, 34(3):276–280.
- Sola, J. (2015). Quaternion kinematics for the error-state Kalman filter. Available online at <http://www.iri.upc.edu/people/jsola/JoanSola/objectes/notes/kinematics.pdf>.

- Yeh, K. C. and Liu, C.-H. (1982). Radio wave scintillations in the ionosphere. *Proceedings of the IEEE*, 70(4):324–360.
- You, D. I., Jung, Y. D., Cho, S. W., Shin, H. M., Lee, S. H., and Shim, D. H. (2012). A guidance and control law design for precision automatic take-off and landing of fixed-wing UAVs. In *AIAA Guidance, Navigation, and Control Conference*, page 4674.
- Zolich, A., Johansen, T. A., Cisek, K., and Klausen, K. (2015). Unmanned aerial system architecture for maritime missions. design & hardware description. In *2015 Workshop on Research, Education and Development of Unmanned Aerial Systems (RED-UAS)*, pages 342–350. IEEE.